Intestinal Stem and Progenitor Cells Exhibit Distinct Adaptive Responses to Inflammatory Stress in IBD

Brinda Balasubramanian[1], Shivam Patel[1], Louis Gall[2], Nick Hannan[3], William Dalleywater[1,4] Joerg Huelsken[5,6,7], Carmen Pin[8], Gordon Moran[9] and Paloma Ordóñez-Morán[1,*]

[1] Translational Medical Sciences Unit, Centre for Cancer Sciences, Biodiscovery Institute, School of Medicine, University of Nottingham, Nottingham, UK.

[2] Centre for Systems Modelling & Quantitative Biomedicine (SMQB), University of Birmingham, Birmingham, UK.

[3] Translational Medical Sciences, Biodiscovery Institute, School of Medicine, University of Nottingham, Nottingham, NG7 2RD, UK.

[4] Cellular Pathology Department, Nottingham University Hospital, Nottingham, UK.

[5] École Polytechnique Fédérale de Lausanne (EPFL), ISREC (Swiss Institute for Experimental Cancer Research), 1015, Lausanne, Switzerland.

[6] Agora Cancer Research Center, Lausanne, Switzerland.

[7] Swiss Cancer Center Léman, Lausanne, Switzerland.

[8] Systems Medicine. CPQP. Clinical Pharmacology and Safety Sciences, R&D. AstraZeneca. Cambridge, UK.

[9] Translational Medical Sciences, School of Medicine, Faculty of Medicine and Health Sciences, University of Nottingham; NIHR Nottingham Biomedical Research Centre, Nottingham, UK.

* Corresponding author: Paloma Ordóñez-Morán, paloma.ordonezmoran@nottingham.ac.uk

Abstract

Background

Intestinal epithelial stem cells (SCs) and their transit-amplifying (TA) progeny are critical for mucosal repair and regeneration. However, their behaviour under chronic inflammatory conditions, such as those observed in Inflammatory Bowel Disease (IBD), remains incompletely understood.

Methods

We investigated the impact of chronic inflammation on intestinal stem/progenitor cells by integrating bulk RNA sequencing from the largest IBD biopsy cohort to date with single-cell transcriptomic analysis and experimental assays using patient-derived intestinal organoids.

Results

Active inflammation was associated with a reduction in canonical LGR5^{+} intestinal stem cells and a concurrent expansion of OLFM4^{+} populations, consistent with an inflammation-induced epithelial repair program. Notably, SC/TA cells from both inflamed and non-inflamed IBD tissues exhibited persistent transcriptional changes that were distinct from those in healthy controls. Single-cell analysis identified transcriptionally heterogeneous SC/TA subpopulations, including a previously uncharacterized inflammation-associated cluster enriched in immune signalling pathways. Pseudotime trajectory analysis demonstrated a shift in differentiation toward deep crypt secretory (Paneth-like) cell lineages under inflammatory conditions.

Conclusions

Chronic intestinal inflammation reshapes the epithelial stem and progenitor cell compartment, promoting altered differentiation and the emergence of immune-responsive epithelial states. These findings highlight the plasticity of the human intestinal epithelium in IBD and point to new avenues for therapeutic strategies aimed at maintaining epithelial integrity during chronic inflammation.

Key words: inflammation, stem cells, progenitors, regeneration, gene expression, Inflammation Bowel Disease, organoid, BEST4, biomarkers.

Introduction

Inflammatory Bowel Disease (IBD) is increasingly recognized by the World Health Organization as a major global health concern, especially given its rising prevalence in high-income countries and growing incidence among younger populations [1–3]. IBD encompasses chronic, relapsing-remitting inflammatory disorders of the gastrointestinal tract, with Crohn's disease (CD) and Ulcerative Colitis (UC) being the primary subtypes. These conditions are driven by an abnormal immune response directed at the intestinal lining, resulting in symptoms such as abdominal pain, diarrhea, fatigue, and weight loss. Over time, approximately 70% of individuals with CD and 20–30% of those with UC require surgical intervention due to complications like strictures, fistulas, abscesses, or failure of medical therapy and malignancy [2,3]. Although the exact aetiology of IBD remains unresolved, current evidence supports a multifactorial origin involving genetic susceptibility, environmental triggers, and immune system dysregulation.

During chronic inflammation, epithelial cells are persistently exposed to pro-inflammatory cytokines and oxidative stress, leading to the activation of signalling pathways such as Hippo-YAP1 and Wnt/β-catenin, which are crucial for maintaining intestinal homeostasis[4–6]. This inflammatory environment compromises the gut barrier by altering epithelial function and increasing tissue permeability, thereby intensifying immune responses [7,8]. These changes negatively impact the proliferation of intestinal stem cells (SC) and transit-amplifying progenitors (TA), while also promoting cell death, ultimately weakening epithelial integrity [9]. SC, which reside at the intestinal crypts, are essential for sustaining epithelial renewal by generating TA that divide and differentiate into the diverse mature cell types lining the intestine [10–12]. It is unclear how SC and TA (SC/TA) attempt to repair or adapt to the inflammatory

75 environment, or what specific signals drive their response in a timely manner in healthy and
76 IBD tissue. It is particularly relevant to know how these cells adapt under stress: whether they
77 shift towards rapid proliferation to replace damaged cells, lean towards self-renewal to
78 preserve the stem cell pool or undergo differentiation.

79 Bestrophin-4 (BEST4)$^{+}$ cells, are a subpopulation of mature absorptive epithelial cells
80 characterized by the expression of the ion channel BEST4[13]. These cells have an important
81 physiological relevance because their unique gene expression profile shows that they have a
82 specialized functions in pH regulation, electrolyte transport, antimicrobial defense, and
83 immune communication[14]. BEST4^{+} cells are emerging as an important cell type in IBD and
84 their loss in inflammation has been reported[14–16], Disruptions among BEST4^{+} cells could impact
85 barrier function, antimicrobial defense, and local immune environments, processes highly
86 relevant to IBD pathophysiology. However, the underlying mechanisms, functional
87 consequences, and potential for barrier permeability and regeneration remains unclear. One
88 of the main reasons for limited progress in this area is the absence of BEST4^{+} cells in mice[17–
89 20]. Integrating them into our human studies of SC/TA populations is relevant for better
90 understanding the origins of BEST4^{+} as they may arise from distinct stem or transit-amplifying
91 cells and understanding their role during chronic inflammation. Overall, the functional
92 relevance of SC/TA and BEST4^{+} cells and its dynamic changes in IBD could reveal key insights
93 into tissue repair, novel therapeutical approaches and the understanding of IBD progression.

94 In this study, we set out to identify the dynamic molecular response of intestinal SC, TA and
95 BEST4^{+} epithelial cell types during inflammation by comparative analysis of omics data and
96 experimental approaches using IBD patients tissue data, DSS-treated UC mouse models and
97 IBD patient-derived organoids (PDOs). Using our multimodal approach, we assessed changes
98 in cell type markers, identified biological processes, and pathway modulations associated with
99 inflammation. Our approach offers the first evidence in a controlled setting to trace molecular
100 signatures and adaptive responses of distinct epithelial molecular clusters in relation to

101 inflammation severity, providing valuable insights into how inflammatory processes disrupt
102 SC/TA epithelial function and contribute to IBD progression. Modulation of these cell types
103 reflects a shift in stemness and differentiation pathways, where specific OLFM4^{+} SC/TA cells
104 increasingly remain in a proliferative state under heightened inflammation, rather than
105 progressing toward full epithelial maturation. Moreover, BEST4^{+} mature cells showed a slight
106 increase in low-inflammation tissue, however, their numbers were significantly downregulated
107 under high inflammatory conditions. These cells may play a regulatory role in maintaining
108 epithelial homeostasis and their reduction during severe inflammation could contribute to
109 disease progression in IBD. This epithelial remodelling highlights a potential pathogenic
110 imbalance between stemness and differentiation in both inflamed and non-inflamed IBD
111 epithelium. Furthermore, we detected that the differentiation trajectory of IBD stem cells is
112 skewed toward the deep crypt secretory cell lineage, also referred to as colonic Paneth-like
113 cells, indicating an aberrant differentiation process. Collectively, our findings demonstrate for
114 the first time how intestinal stem cell and progenitor epithelial cell types actively engages in
115 adaptive responses to inflammation, balancing proliferation and differentiation processes that
116 are critical for tissue repair and epithelial.

117

118 Results

119 **Profiling epithelial cell heterogeneity based on inflammation severity**

120 To understand the epithelial cell heterogeneity under varying degrees of inflammation, we
121 investigated the cell type distribution based on macroscopic appearance of IBD tissue. To that
122 end, we utilized bulk-RNA sequencing (RNAseq) data from the largest cohort of IBD patients'
123 biopsies analysed to date (IBD Plexus Study of a Prospective Adult Research Cohort, SPARC
124 IBD) (UC=1,097, CD=2,138) of the Crohn's & Colitis Foundation IBD Plexus program which

125 includes clinical, genetic, molecular, environmental, and patient-reported outcomes from
126 individuals with CD or UC[21] (Figure S1A).

127 We employed deconvolution analysis using CIBERSORTx to quantitatively estimate the
128 epithelial, immune, and stromal cells type proportion with a signature matrix constructed using
129 single cell-RNAseq (sc-RNAseq) data from human intestine as reference[15] (Figure 1A and
130 S1B). The overall quantitative relative abundance of cycling TA, and immature enterocytes (2)
131 pool involved mainly in metabolic processes, decreased with increasing inflammation severity
132 reflecting an altered capacity within the epithelial lining. However, there was an increase in
133 immature enterocytes (1), which are involved in tight junction repair during inflammation[22].
134 This rise may be a compensatory mechanism, aiming to restore barrier integrity despite the
135 diminished support from the TA pool. In parallel, M cells, key players in mucosal immune
136 surveillance, were significantly enriched in inflamed tissues, consistent with heightened
137 immune activity (Figure 1B and S1C). Well-characterized SC, TA, BEST4^{+} cell type markers
138 and/or Wnt pathway target genes, such as *LGR5*, *AXIN2*, *EPHB2, ASCL2, PROM1*, *LRIG1* and
139 *BEST4*, were significantly lower expressed in inflammation vs normal or possible inflammation
140 of UC (Figure 1C, D) and CD (Figure S1D, E). In contrast, *OLFM4*, a key SC/TA marker strongly
141 associated with cell proliferation and rapid cellular renewal [23], increased as inflammation
142 intensified (Figure 1C, D and S1D, E). Clusterin (*CLU*) 'revival stem cell' pool marker involved
143 in tissue regeneration after injury[24] increased with inflammation severity (Figure 1C and S1D).
144 This suggested an adaptive response, where OLFM4^{+} proliferative cells in IBD tissue aim to
145 counterbalance the loss of epithelial integrity caused by inflammation.

146 To understand better the healthy SC/TA response to an initial signal of injury and compare it
147 to IBD tissue response, we analysed the DSS-mouse model bulk-RNAseq[25] (GSE22307), and
148 the sc-RNAseq [26](GSE264408) data where EPCAM^{+} epithelial cells were extracted from the
149 total cell population (Figure 1F). SC/TA and Wnt gene expression markers as *Lgr5*, *Sox9*,
150 *Ephb2* and *Axin2* decreased over the course of inflammation, indicating a general decline

151 within the intestinal tissue *in vivo* that are altered by an inflammatory stimulus. Lgr5^{+} stem cells
152 tend to recover at day 4, reflecting an initial response to restore this pool in healthy epithelium.
153 We identified an upregulation *of Clu* expression correlated with rising levels of S100 Calcium-
154 Binding Protein A9 (*S100A9*), a biomarker commonly upregulated in inflammatory diseases[27]
155 (Figure 1E-G). Interestingly, Olfm4 increased at the protein level as inflammation intensified in
156 the small intestine of DSS-treated mice (Figure 1H). These findings show how SC/TA pools
157 balance regeneration and barrier integrity during inflammation in healthy and IBD tissue.

158

159 **Characterization of epithelial cell types in IBD vs healthy tissue using a 3D patient-**
160 **derived organoid model**

161 To investigate epithelial cell heterogeneity in IBD cells in absence of active inflammatory
162 conditions, we derived 3D-intestinal epithelial organoids from IBD patient's biopsies that retain
163 the unique genetic and phenotypic characteristics of patient's tissue that had been affected
164 by chronic inflammation[28–30] (Figure 1A). The expansion of these cells allowed us to create
165 simplified *in vitro* IBD models that maintain active stem cell niches, and ongoing differentiation
166 characteristic of non-inflamed (IBD normal) patients' cells (Figure 2A). We performed bulk-
167 RNAseq of healthy (hPDOs) derived from healthy individuals and IBD-PDOs derived from IBD
168 patient's tissue: IBD patient 89 (P89), P90 and P99. All the IBD-PDOs exhibited similar gene
169 expression profiles, with P99 displaying a more pronounced inflammatory phenotype
170 (Supplementary Figure 2A-C). Healthy and IBD-P99 organoids of early (passage 3) and late
171 passages (passage 10) were sequenced to assess potential differences in molecular
172 characteristics over time in culture. This approach allowed us to determine that passage
173 number did not have a major influence on their gene expression profile (Figure 2B-I and S2A).

174 The RNA-seq data was first validated by analysing previously reported IBD-PDOs
175 biomarkers[31]: downregulated genes (*AQP8*, *CD177*, *PIGR*, *PLA2G2A*, and *ZNF257)* (Figure

176 2B) and upregulated genes (*FLNA*, *HLA-DRA*, *HLA-DRB1*, *KCNJ3*, *LYZ*, *MSN*, and *SLITRK6)*
177 of IBD- vs hPDOs (Figure 2C). We identified 80 upregulated and 20 downregulated DEGs in
178 IBD- vs hPDOs (fold change cutoff=5, p-value<0.05), where IBD-PDOs exhibited upregulation
179 of genes involved in inflammatory pathways, such as cytokines and chemokines as IL-1β and
180 IL-6 (Figure 2D, E). By Signalling Pathway Impact Analysis, we found other enriched pathways
181 such as Wnt, PI3K-Akt and Ras, and downregulated pathways such as TGFβ signalling in IBD-
182 PDOs vs hPDOs reflecting the impact of chronic inflammation on intestinal non-inflamed IBD
183 epithelial tissue which included metabolic shifts, epithelial barrier function and, key signalling
184 pathways involved in regeneration (Figure 2F and S2B).

185 To quantify and compare cell type content in both type of PDOs, we employed deconvolution
186 analysis using CIBERSORTx with a signature matrix constructed using sc-RNAseq data from
187 healthy human intestinal epithelial cells as reference[32]. We found that TA and Paneth cells
188 were increased in IBD- compared to hPDOs while BEST4^{+} and enterocyte pools were
189 decreased (Figure 2G). By qPCR we detected a significant increase of *OLFM4* in IBD-
190 compared to hPDOs, however we found no significant change in *LGR5 and CLU* expression
191 (Figure 2H and S2C). Moreover, the bulk-RNAseq gene expression analysis confirmed the
192 significant upregulation of *OLFM4* and *EPHB2* (TA and Wnt target gene, respectively) in IBD-
193 vs hPDOs (Figure 2I).

194 IL-22 is a cytokine that has a pivotal role in enhancing epithelial proliferation and stem cell-
195 driven regeneration [33,34] which are essential processes disrupted during IBD. So, we analysed
196 IL-22 pathway activation in human hPDOs to study OLFM4^{+} proliferative cells function in repair
197 and regenerative intestinal mechanisms[35,36]. To that end we extracted EPCAM^{+} epithelial cells
198 from the total population of sc-RNAseq data[35] (GSE189423) and analysed the DEGs (Figure
199 2D-G). Interestingly, one of the top upregulated genes was *OLFM4* (Figure 2I) which we further
200 validated by qPCR in our IL-22 treated vs control hPDOs. In parallel, IL-22 treatment reduced
201 goblet cells detected by the decrease of *MUC2* expression marker (Figure 2J, K). Our findings

202 identify OLFM4^{+} pool as key players of IBD epithelium and in epithelial repair mechanisms
203 induced in healthy epithelium.

204

205 **Characterization of SC/TA and BEST4^{+} pools in healthy and IBD non-inflamed and**
206 **inflamed tissue.**

207 We next analysed the heterogeneity of intestinal SC/TA and BEST4^{+} cell pools as these are
208 key epithelial cells involved in regeneration by using publicly available sc-RNAseq data[15,37]. We
209 extracted EPCAM^{+} epithelial cells from IBD non-inflamed (IBD normal) and inflamed tissues,
210 and from healthy individual biopsies (UC=18, healthy=12 and, CD=46, healthy=25). Cell type
211 annotations were standardized by using epithelial reference dataset (Figure 3A) (GSE185224)
212 and labels of the cell types were transferred into the selected sc-RNAseq data using SingleR,
213 ensuring unbiased labelling across datasets[38] (Figure 3B and S3A). We then extracted SC/TA,
214 and BEST4^{+} cell populations data, the latter being part of the enterocyte lineage directly
215 derived from progenitors. We separated the data into healthy, non-inflamed (or normal), and
216 inflamed groups, and observed a decrease in the SC/TA and BEST4^{+} pools in IBD inflamed
217 tissue compared to healthy samples (Figure 3C and S3B).

218 Next, we performed principal component analysis on the variable features in a total of 11,268
219 cells for UC and 9,894 cells for CD datasets. We identified clusters using the Louvain algorithm
220 with results visualised via Uniform Manifold Approximation and Projection (UMAP). This
221 analysis resulted in 19 transcriptionally distinct UC clusters, and 13 CD clusters highlighting
222 the functional heterogeneity and roles of SC/TA and BEST4^{+} cell types (Figure 3D and S3C).
223 Clusters were further classified based on the cell type (BEST4^{+}, SC and TA) (Figure 3E and
224 S3D) and health status of the source tissue (healthy, non-inflamed and inflamed) (Figure 3F
225 and S3E). The relative abundance of these clusters was evaluated based on cell types and
226 health status (Figure 3G, H and S3F, G). We used the top 50 gene markers of each cluster to

227 identify representative pathways, cell types and gene ontologies enrichment analyses (Table
228 S1). Of all the computed clusters, UC-C1, -3, -4, -7, -11, -12, -17, -18 and CD-C1, -5, -8, -12, -
229 13, aligned clearly with known biological processes so we further refined the markers specific
230 to these clusters (Figure 3I, J and S3H, I). Interestingly, we identified six gene clusters (UC-
231 C1, -3, -12 and CD-C1, -5, -8) that predominantly consisted of TA cells (Figure 3G and S3F)
232 highly enriched in MKI67^{+} proliferative states, showing high expression of proliferative markers
233 like *PTTG1*, and *UBE2C* (Figure 3I-K and Table S1). The gene clusters UC-C1, -3 and CD-C1,
234 -5 reflected enrichment of genes associated with cell division, M-phase of cell cycle, and
235 microtubule cytoskeleton organization in mitosis. UC-C12 and CD-C8 were enriched in
236 markers of S-phase, DNA synthesis and replication (Figure 3L and S3H).

237 Furthermore, we observed that IBD-PDOs vs hPDOs had higher expression levels of the top
238 50 proliferative markers, likely highlighting these cells' role in adaptive proliferative
239 mechanisms (Figure S3I). We further analysed the top 50 markers from these clusters in the
240 DSS-mouse model (GSE22307) and observed that the MKI67^{+} cluster markers showed a
241 biphasic proliferative response of healthy cells to cellular damage. This response was
242 characterized by an initial decrease in proliferation, followed by a subsequent replenishment
243 of proliferative cells, surpassing the original gene expression levels (Figure S3J, K). We further
244 validated increased expression of *OLFM4* in IBD inflamed and non-inflamed vs healthy tissue
245 in most of the clusters (Figure S3L). Together these findings highlight relevant and unique
246 dynamics of these clusters in the SC/TA and BEST4^{+} pools during inflammation in healthy and
247 IBD epithelium.

248

249 **An immune-enriched gene cluster present exclusively in SC/TA and BEST4^{+} pools of IBD**
250 **inflamed tissues**

251 We further investigated clusters UC-C18 and CD-C12 as these were predominantly composed
252 of IBD cells and were absent in healthy tissue (Figure 3H and S3G). Enrichment analysis of the
253 top 50 gene markers from each cluster showed their involvement in immune-related pathways
254 such as IL-17, TNFα, NF-kB and Oncostatin M (Figure 4A and S4A). Notably, top marker genes
255 such as *ANXA1*, *REG4*, *TFF1*, and *TIMP1,* previously linked to mucosal healing, epithelial
256 restitution, and regeneration, were highly expressed within these clusters[39–42]. Markers for UC:
257 *ANXA1*, *REG4*, *TFF1*, *CD55*, *TIMP1*, and *PI3; and* for CD: *PI3, IGGL5, REG4, DUOXA2, TIMP1,*
258 *and CXCL1)* were chosen for further analysis as their expression was specific to UC-C18 and
259 CD-C12, respectively (Figure 4B and S4B). These markers were present in SC, TA and
260 BEST4^{+} cell types (Figure 4C, D and S4C, D). In SPARC IBD UC and CD data, the top genes
261 of UC-C18 and CD-C12 were able to stratify patients according to their macroscopic
262 appearance. Moreover, the average expression of these genes was significantly upregulated
263 in inflammation and possible inflammation groups when compared to the normal group.
264 Interestingly, this upregulation was also statistically significant in inflammation vs possible
265 inflammation group (Figure 4E, F and S4E, F). We observed that the average gene expression
266 of this signature increased with inflammation status from day 0 to 6 of DSS-treated mice
267 (GSE22307) (Figure 4G and S4G). In IL-22 treated hPDOs sc-RNAseq data (GSE189423) we
268 found that *ANXA1*, *CD55*, *PI3* and *TIMP1* were increased in IL-22 treated human organoids vs
269 control and all of them were expressed in LGR5^{+} stem cells (Figure 4H, I). Hence, the UC-C18
270 and CD-C12 gene signature, represent inflammatory biomarkers of the epithelial
271 compartment, and show promise in molecularly stratifying IBD patients based on their
272 macroscopic appearance.

273

274 **Inflammation-Dependent Adaptive Dynamics of Epithelial Cells Categorized by a Novel**
275 **Inflammation-Linked Gene Signature Associated with Disease Severity in IBD**

276 We aimed to identify a reliable inflammation-associated gene signature to molecularly stratify
277 patient samples according to the degree of inflammation and understand epithelial dependent
278 inflammation dynamics. We curated an inflammation-related gene list (n=476) (Table S2) and
279 compared their average gene expression in different clinical classifications of inflammation
280 severity. We categorized the samples by clinical disease activity and found not significant
281 differences between the groups defined by Mayo score for UC (mild, moderate, severe, and
282 remission) and short Crohn's Disease Activity Index (sCDAI) for CD (Figure 5A and S5A).
283 However, when samples were categorized by macroscopic appearance recorded during
284 endoscopy of IBD patients (normal or non-inflamed, possible inflammation, and inflammation)
285 they formed three significantly distinct groups (Figure 5B and S5B). We then confirmed that
286 *S100A9* gene expression was significantly upregulated in the inflamed samples when
287 compared to possible inflammation or normal ones (Figure 5C and S5C). We further confirmed
288 S100A9 protein upregulation in inflamed vs non-inflamed regions of IBD patient's tissue
289 samples (Figure 5D).

290 We validated the categorization of these groups by using an inflammation-related gene
291 signature (n=42) from a prior UC study[15] (Figure S5D, E). In addition to the expected
292 upregulation of inflammatory genes in the inflamed vs normal group, we found that possible
293 inflammation category also showed elevated expression of inflammatory markers compared
294 to the normal group suggesting an underlying genetic predisposition to inflammation that is
295 not clear in tissue macroscopic assessments. Overall, we found that the macroscopic
296 appearance is a reliable classifier of inflammation severity, hence, it was maintained for further
297 analyses.

298 We then performed differential gene expression analysis to compare the inflammatory profile
299 across these groups using the curated inflammation-related gene signature (n=478). In UC,
300 we found 112 differentially expressed genes (DEGs) between inflammation vs normal samples,
301 38 DEGs between possible inflammation vs normal samples, and 29 DEGs between

302 inflammation vs possible inflammation samples (Table S3). A Venn diagram illustrated that 26
303 genes (26-GIN-UC) were consistently differentially expressed across all three comparisons
304 (Figure 5E). In addition, multiple dimensionality (MDS) analysis showed that this gene
305 signature was effective in clustering the samples according to the clinical classifier of their
306 macroscopic appearance highlighting their potential in distinguishing inflammation (Figure 5F).
307 In CD, we found 380 DEGs between inflammation vs normal samples, 304 DEGs between
308 possible inflammation vs normal samples and 35 DEGs between inflammation vs possible
309 inflammation samples A Venn diagram illustrated those 30 genes (30-GIN-CD) shared among
310 the three comparisons and MDS plots demonstrated effective sample stratification (Table S3
311 and Figure S5F, G). To further evaluate both gene signatures (26-GIN-UC and 30-GIN-CD),
312 we performed unsupervised hierarchical clustering analysis on the SPARC IBD cohort which
313 aligned with macroscopic appearance effectively clustering the samples according to the
314 inflammation category. Enrichment analysis of these two gene signatures showed strong
315 representation of inflammatory response pathways as TNFα and IL-6/JAK/STAT (Figure 5G, H
316 and S5H, I). Comparison of inflamed vs normal samples from the proteomics SPARC IBD
317 dataset (UC and CD) confirmed that members of inflammatory pathways such as interleukins
318 IL-10, -24, -17 were amongst the significantly differentially expressed proteins (p-value < 0.05)
319 (Figure 5I and S5J). Protein-protein interaction analysis showed that proteins related to focal
320 adhesion, extracellular matrix reorganisation were downregulated, whereas proteins related to
321 pro-inflammatory and profibrotic mediators were upregulated (data not shown).

322 We further validated these gene signatures in three different transcriptomic datasets of dextran
323 sulphate sodium (DSS)-treated UC mouse model that tracks inflammatory responses and
324 disease progression over time[43]. We identified the upregulation of the 26-GIN-UC and 30-GIN-
325 CD signatures with increasing inflammation, observing the onset, peak, and resolution of
326 inflammation in a time-dependent manner (Figure 5J-L, and S5K).

327 We then evaluated the effectiveness of the new identified gene signatures in stratifying IBD
328 samples according to inflammation degree. First, we performed unsupervised hierarchical
329 clustering on SPARC IBD UC samples, identifying five distinct groups based on their UC-C18
330 gene expression profiles. This clustering reflected the underlying biological patterns
331 (endoscopic assessment/macroscopic appearance) thereby providing a novel unbiased
332 approach for IBD samples stratification. We found that these groups corresponded to varying
333 inflammation potential grades, ranging from 1 to 5, with 1 representing low inflammation and
334 5 representing severe inflammation. We validated this classification with the average
335 expression of the 26-GIN-UC (Figure 5) and UC-C18 gene signatures, which showed a
336 progressive increase with the degree of inflammation, confirming the appropriate stratification
337 of the samples (Figure 6A-C). Notably, *S100A9*, showed a significant upregulation in the most
338 inflamed samples, reinforcing the robust and unbiased framework for classifying IBD samples
339 based on inflammation degree (Figure 6D).

340 We overlaid the average expression of specific SC/TA and differentiated cell markers with both
341 inflammatory signatures. *LGR5* expression, showed varying levels in different inflammation
342 degrees, with an overall decrease in the highest inflammation degree 5 and weak negative
343 correlation with (r = -0.085) with UC-C18 signature. The spline curve model shows the dynamic
344 shift in *LGR5* expression in the different inflammation degrees (Figure 6E and S6). *OLFM4*
345 expression exhibited a subsequent upregulation in degrees 3 to 5 with an overall positive
346 correlation (r = 0.579) with the UC-18 signature (Figure 6F and S6). Similarly, the revival stem
347 cell marker *CLU* increased with severity of inflammation with positive correlation (r = 0.542)
348 (Figure 6G and S6), while *BEST4* was upregulated in degree 2 but its expression gradually
349 decreased in degree 3 and 4 (Figure 6H). *VIL1*, gene expressed in enterocytes lining the
350 intestinal villi and crypts, showed a dynamic expression from degree 2 to degree 4 (Figure 6I).
351 *AVIL*, gene marker for brush border integrity and actin dynamics and *FABP1* enterocyte
352 marker were both decreased upon severity of inflammation (Figure 6J, K). We observed that

353 proliferation markers such as *PCNA* exhibited a general increase when compared degree 5 vs
354 degree 1 (Figure 6H) that reflects the balance between inflammation-induced epithelial injury
355 and the subsequent regenerative response. Moreover, we observed a similar trend of negative
356 correlation of *BEST4*, *VIL1*, *AVIL* and *FABP1* with UC-18 expression (r = -0.3, -0.35, -0.536, -
357 0.496, respectively). (Figure S6). We obtained very similar results for CD dynamic shifts (CD-
358 C12, and 30-GIN-CD) (Figure S7). We evaluated the robustness of these signature using
359 patient level hold out test our models performed very well for "Normal" samples, while
360 classification of inflamed states was more modest and the intermediate "Possible
361 inflammation" cases were not well predicted as it likely represents a heterogeneous mix of
362 early, partial, or ambiguous lesions, and may also capture endoscopic uncertainty (Figure
363 S7p,q). To address this, we also applied unsupervised clustering of the gene signature
364 followed by dendrogram-based cutting to derive an alternative, data-driven ordering (Figure
365 6). This approach produced a molecularly defined progression of five groups that may better
366 reflect underlying biology. This complementary analysis highlights that transcriptomic ordering
367 can resolve heterogeneity within inflamed states. In addition, we also evaluated whether
368 clinical parameters had an effect on the ability of this gene signature to stratify inflammation.
369 We found that the gene signature score remained strongly associated with macroscopic
370 appearance after adjusting for sex, race, and smoking status, with direction and magnitude
371 consistent across models for both UC and CD. None of the covariates materially altered the
372 effect of the signature, indicating that the association is independent of demographic or
373 smoking-related factors (Supplementary Table S5, S6).

374 The combination of scatter plots and spline curve model provided a comprehensive approach
375 in understanding how the average expression of UC-C18 and CD-C12 gene signature reflects
376 dynamic changes in different cell type markers. While scatter plots offer a more rigid, point-
377 by-point correlation, spline curves capture smoother, more continuous transitions in
378 expression patterns within our patient stratifications. Together, these methods show

379 inflammation-dependent SC/TA and BEST4^{+} cells dynamics and demonstrate that these pools
380 derived UC-C18 and CD-C12 gene signatures reflect both broad and subtle dynamic shifts
381 across different inflammation degrees.

382

383 **Exploring molecular mechanisms in IBD by data integration of UC and CD sc-RNAseq**
384 **datasets**

385 We then performed integration of the epithelial cell compartments of SCP259 (UC) and
386 SC1884 (CD) to ensure comparability across both IBD subtypes, UC and CD. This revealed
387 overlapping epithelial cell populations (Figure S8A-D). We applied standardised automated
388 cell annotations with CellTypist, referencing the pan-gastrointestinal (pan-GI) atlas, with minor
389 manual adjustments (Figure S8E). This analysis revealed a marked depletion of colonocytes
390 in inflamed samples, accompanied by a notable expansion of deep crypt secretory cells (DCS),
391 which are thought to represent the colonic equivalent of small intestinal Paneth cells (Figure
392 S8F).

393 To confirm the combined changes associated with inflammation in both IBD subtypes, we
394 performed unsupervised clustering of gene expression profiles based on disease status,
395 grouping inflamed UC and CD samples into “inflamed”, “non-inflamed” category and “healthy”
396 samples (Figure S8G). This analysis identified a core set of 20 top differentially expressed
397 genes that were consistently upregulated in inflamed UC/CD but exhibited minimal expression
398 in non-inflamed and healthy samples (Figure S8H). We used these genes to create an
399 inflammatory gene score to assess cell-type-specific expression patterns, which revealed that
400 they are predominantly expressed in the DCS population, with limited expression across other
401 cell types (Figure S8I). Transcription factor activity mapping across various cell populations
402 further identified NFκB activation in DCS as a key feature of inflamed state, consistent with
403 findings from the differential expression analyses comparing IBD inflamed vs non-inflamed

404 cells in DCS and stem cells (Figure 7A-D). Trajectory analysis indicated that the differentiation
405 trajectory of intestinal SCs is disrupted during inflammation, with a skewing toward DCS
406 lineages (Figure 7E). Genes related to DCS trajectory were expressed higher in inflamed tissue
407 relative to the healthy samples (Figure 7F).

408 Together, these findings suggest that inflammation disrupts normal epithelial differentiation,
409 driving SCs toward a DCS-like fate characterized by expression of pro-inflammatory genes.
410 Notably, the data identifies biomarkers of inflammation-associated stem cell reprogramming in
411 the colonic epithelium.

412

413 Discussion

414 Accurately evaluating inflammation severity in IBD remains a clinical challenge. Existing
415 approaches such as symptom-based scores and biomarker assessments, frequently lack the
416 sensitivity and specificity needed to reliably reflect the extent of inflammation. Endoscopy,
417 often followed by histological examination, remains the gold standard but is invasive, costly,
418 and not readily accessible in all settings. This underscores the urgent need for robust, non-
419 invasive, and reproducible molecular methods to assess inflammation in IBD. Such tools are
420 crucial for improving patient stratification, guiding treatment decisions, and deepening our
421 understanding of epithelial and immune-driven tissue pathology[44–46]. Traditional clinical indices
422 obtained by endoscopies, such as the sCDAI for CD and the Mayo score for UC, are widely
423 used but often fail to reflect the molecular and cellular heterogeneity of inflammation observed
424 at the tissue level[47,48]. In this study, we found that macroscopic appearance assessed during
425 endoscopy closely aligned with inflammation-associated gene expression, suggesting its
426 possible future potential to serve as a biologically meaningful classifier of inflammation severity
427 rather than overall disease activity. Through differential gene expression analysis based on
428 macroscopic appearance, we identified distinct inflammation-associated gene signatures for

429 UC and CD. These signatures offer an unbiased approach for stratifying patient samples and
430 provide valuable insights into epithelial cell diversity, regenerative responses, and barrier
431 function across varying degrees of inflammation in IBD disease subtypes. These findings are
432 preliminary and require prospective validation before they can be proposed as clinical tools.

433 Understanding how different epithelial cell populations, including stem and progenitor cells,
434 react to varying levels of inflammation is essential for unravelling the processes of mucosal
435 injury and healing. Our comprehensive profiling of epithelial cell heterogeneity across different
436 inflammation stages reveals significant and coordinated shifts in the different epithelial cell
437 pools. Through a multimodal analytical approach, we observed a reduction in TA cells as
438 inflammation severity increased, a trend previously associated with impaired proliferative
439 capacity during chronic inflammation or skewed differentiation dynamics[16,49]. In contrast, we
440 observed that LGR5^{+} stem cells varied across inflammation duration and intensity, which
441 possibly suggests a constant compensatory mechanism aimed at restoring epithelial barrier
442 integrity. Interestingly, OLFM4^{+} proliferative cells exhibited sustained upregulation during
443 inflammation, reflecting a regenerative response to counterbalance epithelial damage, and this
444 expression remained elevated even in non-inflamed IBD tissue further highlighting the
445 expansion of proliferative stem cells as a hallmark of IBD. Our findings revealed that these
446 dynamics were substantiated in mouse healthy tissue[50], where inflammation led to the
447 decrease of TA pool along with an increase in Clu^{+} and Olfm4^{+} stem-like populations. This new
448 identified epithelial functional plasticity driven by inflammation has potential implications for
449 barrier dysfunction and regeneration.

450 Under inflammatory conditions, the proliferation of SC/TA cells is predominantly regulated by
451 pathways such as Wnt/β-catenin and Ras signalling. These pathways are essential for
452 sustaining the equilibrium between self-renewal and differentiation within the stem cell
453 niche[6,10,51,52]. Inflammatory cytokines such as TNFα and IL-6 are known to enhance the
454 proliferation of intestinal stem cells by activating signalling pathways like STAT3. This

455 activation can amplify the inflammatory milieu and contribute to an excessive proliferative
456 response within the tissue[53–56]. Our mechanistic insights and SC/TA dynamics data indicate
457 that while enhanced proliferation may initially facilitate tissue repair, it can also lead to
458 dysregulation in chronic inflammatory settings. This may result in depletion of the stem cell
459 reservoir or inappropriate differentiation, ultimately weakening the intestinal barrier and
460 contributing to the sustained epithelial injury seen in IBD[36]. Targeting specific proliferation-
461 related pathways within this epithelial clusters may offer therapeutic potential by fine-tuning
462 regenerative responses to improve barrier integrity while avoiding the overactivation that
463 contributes to disease pathology.

464 We found that IBD tissue classified as non-inflamed still exhibits subtle transcriptional and
465 cellular alterations compared to healthy control, suggesting a baseline state of immune
466 activation and epithelial stress even in macroscopically normal regions[16,57]. To explore
467 epithelial cell-type alterations between IBD and healthy tissue in the absence of overt
468 inflammation, we leveraged 3D PDO models, which we confirmed that it recapitulates the
469 cellular composition and regenerative dynamics of the intestinal epithelium[29–31]. IBD-PDOs
470 displayed a distinct epithelial profile compared to hPDOs, including upregulation of
471 inflammatory mediators and SC/TA proliferative markers such as OLFM4. These changes
472 were accompanied by a reduction in differentiated epithelial cell types, such as enterocytes
473 and BEST4^{+} cells, and an increase in Paneth cell populations, suggesting a shift toward a
474 regenerative or stress-associated state. This reinforces the concept that epithelial cells in IBD
475 retain a molecular imprint of inflammation, even in histologically normal areas[16,58,59].
476 Additionally, IL-22 pathway activation in hPDOs showed that OLFM4^{+} cells are activated during
477 epithelial repair, supporting their role as mediators of regeneration in both homeostatic and
478 disease settings. We highlight the utility of PDO models to dissect functionally epithelial
479 alterations in IBD offering insights into therapeutic response.

480 We further characterized SC/TA and BEST4^{+} epithelial clusters uniquely enriched in inflamed
481 IBD tissues but absent in healthy samples. These clusters were significantly enriched for
482 immune-related pathways that are well-established drivers of chronic intestinal inflammation
483 and epithelial remodelling in IBD[60,61]. This enrichment suggests the emergence of
484 inflammation-specific epithelial transcriptional states during active disease. We report here, for
485 the first time, an inflammation-associated epithelial gene signature specific to stem and
486 progenitor cells. This signature successfully stratified patients based on their macroscopic
487 inflammation degree in both UC and CD. The observed enrichment of SC/TA signatures in
488 inflamed tissue aligns with earlier reports of crypt hyperplasia and stem cell activation as
489 hallmark features of IBD pathology[56,62]. Thus, these transcriptional states likely represent
490 inflammation-induced epithelial remodelling programs, offering a refined molecular framework
491 for patient stratification and potential therapeutic targeting of regenerative responses in IBD.

492 Our data suggest that inflammation alters the differentiation trajectory of intestinal stem cells,
493 skewing them toward DCS cell lineages, which are implicated in epithelial barrier maintenance
494 and immune regulation [16]. This shift occurred alongside a relative depletion of colonocyte
495 differentiation and was also evident in non-inflamed IBD-PDOs when compared to healthy
496 controls. This adaptability can be crucial in chronic inflammatory conditions as stem cells must
497 maintain tissue integrity despite continuous stress. However, it also raises questions about
498 long-term consequences, as chronic inflammation can lead to exhaustion or altered
499 differentiation patterns in stem cells, potentially impacting their regenerative capabilities over
500 time[63,64]. These findings reflect a broader epithelial remodelling driven by disrupted lineage
501 commitment. Notably, we identified a core set of inflammation-associated genes highly
502 expressed in DCS, with NF-κB signalling emerging as a prominent regulator that requires
503 direct experimental follow-up for functional validation. This aligns with previous studies
504 highlighting the central role of the NF-κB pathway in mediating epithelial responses after injury
505 and sustaining chronic inflammation[65,66]. Furthermore, NF-κB activation has been shown to

506 modulate Wnt pathway in colonic mouse tissue and specific ablation of RelA/p65 retards crypt
507 stem cell and progenitors expansion[67,68]. Future investigations may help to determine whether
508 modulating this pathway in DCS could lead to new therapeutic opportunities for IBD. However,
509 selectively targeting NF-κB signalling in DCS is technically challenging due to the complex
510 cellular composition of the intestinal mucosa, intestinal region-specific identity, and the broad
511 physiological roles of NF-κB in maintaining epithelial integrity and immune balance[65,66,69].
512 Furthermore, several studies have demonstrated the complex interactions between individual
513 NF-κB subunits in regulating colonic susceptibility to inflammation[69–71]. In addition, off-target
514 modulation could disrupt homeostatic mechanisms, potentially leading to adverse
515 consequences such as impaired wound healing, or dysregulated inflammatory responses.
516 Overcoming these barriers will require advances in targeted delivery systems, and rigorous
517 preclinical validation to ensure safety and specificity for future therapeutic applications.

518 In summary, our findings highlight how inflammation-induced alterations in epithelial stemness,
519 and differentiation contribute to the dysfunction of the intestinal barrier in IBD. The capacity of
520 stem and progenitor cells to adapt under inflammatory stress offers valuable insights for
521 enhancing tissue repair strategies. Targeting these adaptive mechanisms may support the
522 development of novel therapies that sustain epithelial regeneration, minimize disease flares,
523 and foster long-term remission. Understanding the link between epithelial plasticity and
524 specific inflammatory cues may ultimately guide precision treatments aimed at improving
525 clinical outcomes and patient well-being.

526

527 Methods

528 **Ethical Review**

529 The research complies with all relevant ethical regulations and guidelines. Intestinal biopsy
530 samples were obtained from the Queen's Medical Centre of Nottingham (UK) with patient

531 consent from IBD patients and histologically healthy individuals in accordance with ethical
532 guidelines (17/EM/0126).

533 Animal DSS-experiments were performed in accordance with protocols approved by the
534 Service de la Consommation et des Affaires Vétérinaires of Canton Vaud, Switzerland
535 (VD1052/VD1053). The work has been reported in line with the ARRIVE guidelines 2.0. Section
536 expanded in the "Declarations" section.

537

538 **IBD Plexus Cohort**

539 The patient cohort included in this study was derived from the Study of a Prospective Adult
540 Research Cohort with IBD (IBD Plexus Study of a Prospective Adult Research Cohort, SPARC
541 IBD) (UC=1,097, CD=2,138)), a part of the Crohn's & Colitis Foundation IBD Plexus program[21].
542 This includes a geographically diverse research cohort of patients with IBD using standardized
543 data and biosample collection methods and processing techniques. We included patients from
544 the SPARC IBD cohort in our analysis, who had a history of UC and CD and had available bulk-
545 RNAseq of biopsies. We also included plasma proteomics, where applicable, for patients within
546 the cohort. SCDAI for CD and 6-point MAYO for UC patients scores were calculated for
547 patients with sufficient data at enrolment and assigned a disease severity classifier:

Disease Activity	sCDAI	6-point MAYO
Remission	<150	0-1
Mild	150 – 219	2-3
Moderate	220-450	4-5
Severe	>450	6

548 Table 1. SCDAI for CD and 6-point MAYO for UC patients scores for disease activity
549 classification.

550

551 **Data acquisition for bioinformatic analysis**

552 All the data processing and analysis was done in RStudio (Version 4.2.0 and 4.3.0) or Python.

553 IBD Plexus data

554 The raw counts of bulk-RNAseq of UC and CD patients derived from biopsy samples within
555 the SPARC IBD cohort were batch corrected using *Combat_seq*, followed by normalisation
556 and log transformation. Multi-dimensionality Scaling (MDS) analysis was performed to check
557 the sample distribution. SPARC IBD samples were compared against different levels of
558 histological inflammation: erosions or ulcers (or inflammation) vs normal, erosions or ulcers vs
559 possible inflammation (or non-inflamed) and erosions or ulcers vs possible inflammation, for a
560 curated inflammatory gene list (n=476) (Supplementary Table 2). Differential gene expression
561 analysis for the different groups in IBD Plexus Cohort was conducted using *edgeR*[72] and
562 *limma*[73]. P-values threshold was set at 0.05 and adjusted using the Benjamini-Hochberg
563 method.

564 Human sc-RNAseq data

565 Pre-processed and annotated sc-RNAseq data containing EPCAM$^+$ epithelial cells from human
566 tissue was obtained from Single Cell Portal of the accession numbers SCP259, SCP1884 and
567 the reference dataset from Gene Expression Omnibus (GEO) under the accession number
568 GSE185224. SCP259 contained cells from both non-inflamed and inflamed tissues data from
569 UC, and healthy individuals' biopsies (UC=18, healthy=12). SCP1884 was a comparable
570 dataset with CD patients and normal individuals' biopsies (CD=46, healthy=25). Cells with
571 mitochondrial gene content exceeding 5%, features fewer than 200 and more than 2,500 were
572 excluded to retain the highest quality cells. Each dataset was processed according to standard
573 workflow using *Seurat*[74] (version 5, package in R. Cell annotation was uniformly performed
574 using SingleR to predict labels using the reference dataset. The counts matrix from both the

datasets was used as the query, while the GSE185224 reference counts were used for the reference labels. Cell type labels were predicted using the Wilcoxon differential expression method. The predicted labels were added to the Seurat object and was subset to include only cells with “TA”, “BEST4^{+}” and “SC” labels and this was used for further analysis.

For single-cell dataset integration studies, SCP259 and SCP1884 raw matrices were imported using scanpy (v1.10.4) and cells were filtered to exclude cells with greater than 20% mitochondrial counts and greater than 6000 features. Next, cells were processed through scrublet and predicted doublets excluded. Counts per cell were normalised to a target of $1x10^4$ and then log-transformed. Highly variable genes were selected followed by principle-component analysis (PCA), nearest-neighbour estimation (n_neighbours = 5, n_pcs = 17, knn=True) and UMAP projection followed by leiden clustering (resolution, 0.3). To correct for batch-effects across the two datasets, batch-balanced k-nearest neighbours (bbknn) correction was performed using the ‘Subject’ as batch key and leiden cluster as confounder. PCA, nearest neighbour, UMAP projection and leiden clustering were repeated using the same settings. Automated cell-type annotation was performed using CellTypist majority voting using the Pan-GI cell atlas model (: https://cellgeni.cog.sanger.ac.uk/gutcellatlas/celltypist_models/2_full_healthy_reference_AP_all_organs_finalmodel.pkl). Each leiden cluster was annotated with the predicted cell label. To check the validity of annotation, cluster specific gene expression was ranked, using the Wilcoxon method. In most cases, marker genes accorded with known markers of each subset, but in a few cases (e.g. Stem_2), gene expression suggested misclassification (e.g. Paneth cell) and therefore these labels were manually corrected. In addition, some clusters were merged (e.g. Goblet_1, Goblet_2) where leiden clustering had separated cells of the same type. Trajectory analysis of specific subsets was performed using scfates and decoupler was used for pseudobulk analysis of cell populations across health states to determine differential

gene expression and transcription factor activity. Finally, genemania (genemania.org) was used for network and gene-set functional analysis of differentially expressed genes.

Cluster UC-C18 and CD-C12

The subset data with progenitors' cells for each dataset were handled individually and processed according to standard workflow from the Seurat package in R. Dimensionality reduction and Louvain Leiden clustering (resolution 0.1 -1.5) were carried out and cell lineages were annotated based on enrichment analysis and defined marker gene expression of each cluster.

DSS-treated mouse models sc-RNAseq data

Single-cell RNAseq data was obtained from GSE264408 was utilised to study the cell type changes in normal, acute and chronic mouse models. Raw matrices were loaded for each sample using the Seurat package. Each sample was processed into a Seurat object, applying filters for quality control: cells with 200–4,000 detected genes and mitochondrial content <10% were retained. Metadata including sample identifiers and condition types were added to Seurat objects. Seurat objects for all samples were merged into a single dataset and standard workflow was applied. Data were further harmonized using the Harmony algorithm to correct batch effects, and integrated clusters were identified using shared nearest neighbour graphs and clustering algorithms. To focus on epithelial S/P cells, $Epcam^{+}$ cells were subset (Epcam > 0.5). Dimensionality reduction (UMAP) and clustering were repeated. $Epcam^{+}$ cells were categorized based on “Lgr5” expression into "Lgr5_Positive" and "Lgr5_Negative" groups. Wilcoxon tests assessed differential expression significance across conditions. Visualizations included violin plots and feature plots for key markers.

DSS--treated mouse models microarray transcriptomic data

Raw expression data of GSE22307 and GSE42768 was downloaded from NCBI-GEO platform and log2 normalised using limma package. Similarly, GSE131032 and GSE214600 raw counts

625 data downloaded from same platform. To process raw counts, we used deseq function of
626 Deseq2 package. Z-score was calculated from normalised data to visualize gene expression
627 in either heatmap or spline curve using pheatmap and ggplot2.

628 PDOs sc-RNAseq data

629 Raw sc-RNAseq of IL-22 treated and untreated intestinal human organoids were retrieved
630 GSE189423, merged, and batch effects were corrected using Harmony integration. $EPCAM^+$
631 cells were identified and further analyzed through dimensionality reduction (UMAP),
632 clustering, and marker gene expression profiling. To focus on epithelial stem/progenitor cells,
633 $Epcam^+$ cells were subset (Epcam > 0.5). UMAP and clustering were repeated. $Epcam^+$ cells
634 were categorized based on "Lgr5" expression into "Lgr5_Positive" and "Lgr5_Negative"
635 groups. Wilcoxon tests assessed differential expression significance across conditions.
636 Visualizations included violin plots and feature plots for *ANXA1* and *REG4*.

637 PDOs bulk-RNAseq data

638 RNA collected from healthy (P12) and IBD organoids (P89, P90, P99) and their mRNA was
639 sequenced. A custom pipeline with standard bulk-RNAseq workflow was implemented for
640 quality control, trimming and alignment. Aligned reads were quantified using FeatureCounts.

641

642 **Pathway Enrichment Analysis**

643 Key pathways of the DEGs were performed in MSigDB database using the web tool, Enrichr.
644 Pathways enriched for the differentially expressed proteins in plasma proteomics of SPARC
645 IBD cohort was identified using KEGG database using protein-protein-interaction networking
646 using the web tool, StringDB. Gene Ontology analysis for the cluster makers was performed
647 using web tool, Enrichr. DEGs with an unadjusted p-value < 0.05 were considered significant.
648 For downstream pathway analysis, we further filtered for DEGs with an adjusted p-value (padj)
649 < 0.05 and an absolute log2 fold change > 5. Pathway enrichment was performed using

650 Signaling Pathway Impact Analysis (SPIA) implemented via the iLINCS platform. Non-relevant
651 pathways, such as those associated with viral responses (e.g., COVID-19), were excluded.
652 Pathways related to epithelial biology were retained for interpretation.

653

654 **Deconvolution Analysis**

655 sc-RNAseq dataset from[15] was used to generate a signature matrix which was employed to
656 derive cell proportions in SPARC IBD samples using CIBERSORTx
657 (https://cibersortx.stanford.edu). Cell proportion chart was made using *ggplot2* in R version
658 (4.3.0).

659

660 **Ordinal Logistic Regression Analysis**

661 An ordinal logistic regression model (proportional odds model, polr function in the R package
662 MASS) was used to assess the relationship between a transcriptomic signature score and
663 macroscopic appearance in SPARC IBD samples. The signature score was derived as the
664 mean z-scored expression of differentially expressed genes. Models were adjusted for clinical
665 and demographic covariates (e.g., sex, race, smoking status), as well as an epithelial marker–
666 based score to account for tissue composition. Odds ratios (OR) and 95% confidence intervals
667 (CI) were calculated by exponentiating regression coefficients.

668

669 **Spline curve analysis**

670 The relationship between the degree of inflammation in SPARC IBD data or DSS treatment in
671 mouse model data and gene expression (expressed as the Z score of CPM) was visualized
672 using a generalized additive model (GAM). we used the geom_smooth() function in the R
673 package ggplot2 with the following parameters:

674 y~s(x,bs="cs",k=4)

675 where y represents the Z score (derived from log2 normalized CPM values) and x represents
676 the degree of inflammation. A cubic spline basis (bs = "cs") was used with k=4 to control the
677 smoothness of the fitted curve.

678

679 **DSS-mouse model**

680 To model UC in mice, DSS or placebo was administered in the drinking water to induce acute
681 colitis. C57BL/6 male mice aged 6–10 weeks were used. A solution of 2.5% DSS (w/v) was
682 prepared using autoclaved water and provided to the mice for 6 days. Throughout the
683 experiment, mice were monitored daily for body weight, stool consistency, and rectal bleeding.
684 At the end-point, animals were euthanized, and colonic tissues were collected for
685 histopathology assays. Adult mice were euthanized by inhalation of carbon dioxide (CO_2) for
686 6 minutes, delivered at a displacement rate of 20% of the cage volume per minute, in
687 accordance with approved ethical protocols. No anaesthesia was used prior to euthanasia.

688

689 **PDOs establishment and culture**

690 Human intestinal crypts were isolated from adult tissues using 25 µg/mL of liberase (Roche),
691 embedded into Matrigel (Corning, Cat 356231) and grown into organoids following previous
692 publications[75]. Organoids were routinely tested for mycoplasma contamination and resulted
693 negative. The details of organoid donors used in each experiment are listed in Supplementary
694 Table 4. Human intestinal organoids were cultured in IntestiCult™ Organoid Human Growth
695 Medium or in-house media prepared following previous publications[75,76] and were split once a
696 week by mechanical dissociation and with TryPLE every two weeks.

697

698 **RNA extraction and sequencing of PDOs**

699 RNA was collected from healthy individuals and IBD patient derived organoids embedded in
700 Matrigel in 48-well plates. RNA was extracted using Qiagen RNeasy kit and RNA quality was
701 assessed with the NanoDrop and the RIN score was checked. RNA samples were sequenced
702 by Novogene, Cambridge, UK.

703

704 **Real-time PCR (qPCR)**

705 250 ng of total RNA isolated from healthy and IBD-PDOs was converted to cDNA using
706 Superscript II (Invitrogen). 20 µL of cDNA was diluted in 200 µL of nuclease free water. For
707 analysing gene expression SYBR green (Applied biosystem) was used according to
708 manufacturer's protocol. All genes CT values were normalised with *GAPDH* (housekeeping
709 gene) of each sample independently.

710

Gene	**Forward (5'->3')**	**Reverse (5'->3')**
LGR5	CTTCCAACCTCAGCGTCTTC	TTTCCCGCAAGACGTAACTC
OLFM4	GACCAAGCTGAAAGAGTGTGAGG	CCTCTCCAGTTGAGCTGAACCA
MUC2	ACCCGCACTATGTCACCTTC	GGACAGGACACCTTGTCGTT
CLU	GAGCAGCTGAACGAGCAGTTT	CTTCGCCTTGCGTGAGGT
GAPDH	CTTGAAGGGTGGAGCCCAAAAG	ATGGATGACTTGGCCAG

711 Table 2. List of primers

712

713 **Immunostaining**

714 Paraffin processing from intestinal biopsies

715 Biopsy tissues were fixed in 4% PFA, placed into individual cassettes, and labelled accordingly.
716 Tissue processing was performed using a Leica TP1020, enabling efficient handling of multiple
717 samples. Tissues were exposed to a graded series of methanol solutions (50% to 100%
718 concentration), with each step lasting 1 hour at RT under vacuum and agitation. Following
719 dehydration, tissues were transferred to xylene for 1 hour at RT, again with vacuum and
720 agitation, to remove residual alcohol and prepare the samples for paraffin infiltration.
721 Embedding was carried out in molten paraffin using disposable molds (Embedding machine)
722 while avoiding bubble formation. The embedded tissues were then cooled on the machine's
723 cooling surface until solidification, and the resulting paraffin blocks were subsequently stored
724 at 4°C.

725 Tissue sectioning

726 A water bath was prepared with distilled water at 45°C for tissue sectioning. Meanwhile, the
727 formalin-fixed paraffin-embedded (FFPE) blocks and forceps were chilled on ice. A microtome
728 blade was installed onto the cutting bed with the correct orientation, and the FFPE block was
729 secured in the block holder. Trimming was performed at 10-µm intervals until the desired
730 depth was reached. Sections were then cut at 4 µm, forming a continuous ribbon that was
731 gently transferred to the water bath using forceps. After briefly floating to separate the
732 sections, slides (Superfrost) were used to mount the individual sections for subsequent
733 Immunofluorescence (IF) staining.

734 Immunofluorescence staining

735 Paraffin-embedded tissue sections were placed on slides and dewaxed in xylene to remove
736 residual paraffin. The sections were then rehydrated through sequential ethanol washes
737 (100%, 90%, 80%, and 70%), each for 5 minutes, followed by distilled water. A 0.5 M sodium
738 citrate buffer (pH 6.0) was freshly prepared, brought to a boil in a microwave, and the slides
739 were submerged for 15 minutes before cooling to room temperature. Permeabilization was
740 carried out using 0.5% Triton X-100 for 1 hour, and blocking solution was prepared by

741 dissolving 0.1 g BSA in 10 ml of wash solution (0.1% Triton X-100 in PBS). Primary antibodies,
742 diluted in blocking solution at the below described concentrations, were applied overnight at
743 4°C. Slides were washed three times, then incubated for 1 hour in the dark with secondary
744 antibodies and DAPI (1:500 in blocking solution). After three additional washes using wash
745 solution, coverslips were mounted using 100% glycerol. Imaging was performed using a Leica
746 confocal SPE microscope.

747 Whole mount PDOs immunostaining

748 For immunofluorescence staining of organoids, we followed protocol from[77,78] with slight
749 modifications. Briefly, organoids were harvested in PBS for staining in 1.5 mL Protein Lowbind
750 tube (Eppendorf) coated with 1% w/v BSA solution. Organoids were then fixed with 4% PFA
751 for 1 hour at 4°C followed by centrifugation at 500 xg for 5 minutes. Permeabilization was
752 performed using a solution of PBS with 0.5% Triton X-100 for 30 minutes at room temperature.
753 Organoids were then blocked with a PBS solution containing 0.5% BSA for 30–60 minutes at
754 4°C. Primary antibody incubation was carried out overnight at 4°C on rotating platform using
755 described concentration in table below. The following day, samples were washed three times
756 with PBS and incubated with a secondary antibody mix containing DAPI for 1 hour at room
757 temperature in the dark. After washing secondary antibody (dilution 1:500 of Alexa 488 anti-
758 mouse or Alexa 568 anti-rabbit), organoids were plated in 96-well plate with black wall and
759 clear bottom and imaged using Lecia Confocal SPE.

Antibodies and dyes	**Company**	**Catalog**	**Dilution**
S100A9	Proteintech	26992-1-AP	1:200
DAPI	Scientific Laboratory	D9542-1MG	1:500
OLFM4	Cell Signalling	D6Y5A	1:200
β-catenin	Santacruz Biotech	sc-7963	1:500

760 Table 3. List of antibodies.

761

762 **Data & code availability**

763 The SPARC IBD data are available upon approved application to Crohn's & Colitis Foundation
764 IBD Plexus study (https://www.crohnscolitisfoundation.org/research/plexus). PDOs bulk-
765 RNAseq data and the code done for this manuscript is deposited in Github Repository
766 (https://github.com/brinda-bala/IBDstemcell.git).

767

768 References

769 1. GBD 2017 Inflammatory Bowel Disease Collaborators. The global, regional, and national
770 burden of inflammatory bowel disease in 195 countries and territories, 1990-2017: a systematic analysis
771 for the Global Burden of Disease Study 2017. *Lancet Gastroenterol Hepatol* **5**, 17–30 (2020).

772 2. Banerjee, R., Raghunathan, N. & Pal, P. Managing inflammatory bowel disease: what to do
773 when the best is unaffordable? *The Lancet Gastroenterology & Hepatology* **8**, 396–398 (2023).

774 3. Lamb, C. A. *et al.* Inflammatory bowel disease has no borders: engaging patients as partners
775 to deliver global, equitable and holistic health care. *The Lancet* **404**, 414–417 (2024).

776 4. Gregorieff, A., Liu, Y., Inanlou, M. R., Khomchuk, Y. & Wrana, J. L. Yap-dependent
777 reprogramming of Lgr5+ stem cells drives intestinal regeneration and cancer. *Nature* **526**, 715–718
778 (2015).

779 5. Imajo, M., Ebisuya, M. & Nishida, E. Dual role of YAP and TAZ in renewal of the
780 intestinal epithelium. *Nat Cell Biol* **17**, 7–19 (2015).

781 6. Fevr, T., Robine, S., Louvard, D. & Huelsken, J. Wnt/beta-catenin is essential for intestinal
782 homeostasis and maintenance of intestinal stem cells. *Mol Cell Biol* **27**, 7551–7559 (2007).

783 7. Hollander, D. *et al.* Increased intestinal permeability in patients with Crohn's disease and their
784 relatives. A possible etiologic factor. *Ann Intern Med* **105**, 883–885 (1986).

785 8. Turner, J. R. Intestinal mucosal barrier function in health and disease. *Nat Rev Immunol* **9**,
786 799–809 (2009).

787 9. Dheer, R. *et al.* Intestinal Epithelial Toll-Like Receptor 4 Signaling Affects Epithelial Function
788 and Colonic Microbiota and Promotes a Risk for Transmissible Colitis. *Infect Immun* **84**, 798–810
789 (2016).

790 10. Barker, N. *et al.* Identification of stem cells in small intestine and colon by marker gene Lgr5.
791 *Nature* **449**, 1003–1007 (2007).

792 11. Capdevila, C. *et al.* Time-resolved fate mapping identifies the intestinal upper crypt zone as an
793 origin of Lgr5+ crypt base columnar cells. *Cell* **187**, 3039-3055.e14 (2024).

794 12. Malagola, E. *et al.* Isthmus progenitor cells contribute to homeostatic cellular turnover and
795 support regeneration following intestinal injury. *Cell* **187**, 3056-3071.e17 (2024).

796 13. Ito, G. *et al.* Lineage-Specific Expression of Bestrophin-2 and Bestrophin-4 in Human Intestinal
797 Epithelial Cells. *PLoS ONE* **8**, e79693 (2013).

798 14. Elmentaite, R. *et al.* Cells of the human intestinal tract mapped across space and time. *Nature*
799 **597**, 250–255 (2021).

800 15. Smillie, C. S. *et al.* Intra- and Inter-cellular Rewiring of the Human Colon during Ulcerative
801 Colitis. *Cell* **178**, 714-730.e22 (2019).

802 16. Parikh, K. *et al.* Colonic epithelial cell diversity in health and inflammatory bowel disease.
803 *Nature* **567**, 49–55 (2019).

804 17. Li, H. *et al.* Cross-species single-cell transcriptomic analysis reveals divergence of cell
805 composition and functions in mammalian ileum epithelium. *Cell Regen* **11**, 19 (2022).

806 18. Širvinskas, D. *et al.* Single-cell atlas of the aging mouse colon. *iScience* **25**, 104202 (2022).

807 19. Tsang, D. K. L. *et al.* A single cell survey of the microbial impacts on the mouse small intestinal
808 epithelium. *Gut Microbes* **14**, 2108281 (2022).

809 20. Schumacher, M. A. *et al.* Deep Crypt Secretory Cell Differentiation in the Colonic Epithelium Is
810 Regulated by Sprouty2 and Interleukin 13. *Cellular and Molecular Gastroenterology and Hepatology*
811 **15**, 971–984 (2023).

812 21. Raffals, L. E. *et al.* The Development and Initial Findings of A Study of a Prospective Adult
813 Research Cohort with Inflammatory Bowel Disease (SPARC IBD). *Inflamm Bowel Dis* **28**, 192–199
814 (2022).

815 22. Gassler, N. *et al.* Inflammatory bowel disease is associated with changes of enterocytic
816 junctions. *American Journal of Physiology-Gastrointestinal and Liver Physiology* **281**, G216–G228
817 (2001).

818 23. Van Der Flier, L. G., Haegebarth, A., Stange, D. E., Van De Wetering, M. & Clevers, H. OLFM4
819 Is a Robust Marker for Stem Cells in Human Intestine and Marks a Subset of Colorectal Cancer Cells.
820 *Gastroenterology* **137**, 15–17 (2009).

821 24. Ayyaz, A. *et al.* Single-cell transcriptomes of the regenerating intestine reveal a revival stem
822 cell. *Nature* **569**, 121–125 (2019).

823 25. Fang, K. *et al.* Temporal genomewide expression profiling of DSS colitis reveals novel
824 inflammatory and angiogenesis genes similar to ulcerative colitis. *Physiological Genomics* **43**, 43–56
825 (2011).

826 26. Hong, D. *et al.* Integrative analysis of single-cell RNA-seq and gut microbiome metabarcoding
827 data elucidates macrophage dysfunction in mice with DSS-induced ulcerative colitis. *Commun Biol* **7**,
828 731 (2024).

829 27. Korndörfer, I. P., Brueckner, F. & Skerra, A. The crystal structure of the human
830 (S100A8/S100A9)2 heterotetramer, calprotectin, illustrates how conformational changes of interacting
831 alpha-helices can determine specific association of two EF-hand proteins. *J Mol Biol* **370**, 887–898
832 (2007).

833 28. Nanki, K. *et al.* Somatic inflammatory gene mutations in human ulcerative colitis epithelium.
834 *Nature* **577**, 254–259 (2020).

835 29. Sato, T. *et al.* Long-term expansion of epithelial organoids from human colon, adenoma,
836 adenocarcinoma, and Barrett's epithelium. *Gastroenterology* **141**, 1762–1772 (2011).

837 30. Ootani, A. *et al.* Sustained in vitro intestinal epithelial culture within a Wnt-dependent stem cell
838 niche. *Nat Med* **15**, 701–706 (2009).

839 31. Dotti, I. *et al.* Alterations in the epithelial stem cell compartment could contribute to permanent
840 changes in the mucosa of patients with ulcerative colitis. *Gut* **66**, 2069–2079 (2017).

841 32. Burclaff, J. *et al.* A Proximal-to-Distal Survey of Healthy Adult Human Small Intestine and Colon
842 Epithelium by Single-Cell Transcriptomics. *Cellular and Molecular Gastroenterology and Hepatology*
843 **13**, 1554–1589 (2022).

844 33. Patnaude, L. *et al.* Mechanisms and regulation of IL-22-mediated intestinal epithelial
845 homeostasis and repair. *Life Sci* **271**, 119195 (2021).

846 34. Cineus, R. *et al.* The IL-22–oncostatin M axis promotes intestinal inflammation and
847 tumorigenesis. *Nat Immunol* **26**, 837–853 (2025).

848 35. He, G.-W. *et al.* Optimized human intestinal organoid model reveals interleukin-22-dependency
849 of paneth cell formation. *Cell Stem Cell* **29**, 1333-1345.e6 (2022).

850 36. Lindemans, C. A. *et al.* Interleukin-22 promotes intestinal-stem-cell-mediated epithelial
851 regeneration. *Nature* **528**, 560–564 (2015).

852 37. Kong, L. *et al.* The landscape of immune dysregulation in Crohn's disease revealed through
853 single-cell transcriptomic profiling in the ileum and colon. *Immunity* **56**, 444-458.e5 (2023).

854 38. Aran, D. *et al.* Reference-based analysis of lung single-cell sequencing reveals a transitional
855 profibrotic macrophage. *Nat Immunol* **20**, 163–172 (2019).

856 39. Vong, L. *et al.* Up-regulation of Annexin-A1 and lipoxin A(4) in individuals with ulcerative colitis
857 may promote mucosal homeostasis. *PLoS One* **7**, e39244 (2012).

858 40. Nanakin, A. *et al.* Expression of the REG IV gene in ulcerative colitis. *Laboratory Investigation*
859 **87**, 304–314 (2007).

860 41. Kapsoritakis, A. N. *et al.* Imbalance of tissue inhibitors of metalloproteinases (TIMP) – 1 and –
861 4 serum levels, in patients with inflammatory bowel disease. *BMC Gastroenterol* **8**, 55 (2008).

862 42. Hensel, K. O. *et al.* Differential expression of mucosal trefoil factors and mucins in pediatric
863 inflammatory bowel diseases. *Sci Rep* **4**, 7343 (2014).

864 43. Okayasu, I. *et al.* A novel method in the induction of reliable experimental acute and chronic
865 ulcerative colitis in mice. *Gastroenterology* **98**, 694–702 (1990).

866 44. Ungaro, R., Mehandru, S., Allen, P. B., Peyrin-Biroulet, L. & Colombel, J.-F. Ulcerative colitis.
867 *The Lancet* **389**, 1756–1770 (2017).

868 45. Torres, J. *et al.* Serum Biomarkers Identify Patients Who Will Develop Inflammatory Bowel
869 Diseases Up to 5 Years Before Diagnosis. *Gastroenterology* **159**, 96–104 (2020).

870 46. Honap, S. *et al.* Prevention and interception trials in inflammatory bowel disease: an
871 international taskforce assessment on clinical trial design. *Lancet Gastroenterol Hepatol* S2468-
872 1253(24)00439–4 (2025) doi:10.1016/S2468-1253(24)00439-4.

873 47. Gomollón, F. *et al.* 3rd European Evidence-based Consensus on the Diagnosis and
874 Management of Crohn's Disease 2016: Part 1: Diagnosis and Medical Management. *ECCOJC* **11**, 3–
875 25 (2017).

876 48. Sands, B. E. & Ooi, C. J. A survey of methodological variation in the Crohn's disease activity
877 index. *Inflamm Bowel Dis* **11**, 133–138 (2005).

878 49. Sanman, L. E. *et al.* Transit-Amplifying Cells Coordinate Changes in Intestinal Epithelial Cell-
879 Type Composition. *Dev Cell* **56**, 356-365.e9 (2021).

880 50. Parigi, S. M. *et al.* The spatial transcriptomic landscape of the healing mouse intestine following
881 damage. *Nat Commun* **13**, 828 (2022).

882 51. Heuberger, J. *et al.* Shp2/MAPK signaling controls goblet/paneth cell fate decisions in the
883 intestine. *Proc. Natl. Acad. Sci. U.S.A.* **111**, 3472–3477 (2014).

884 52. Kabiri, Z. *et al.* Wnt signaling suppresses MAPK-driven proliferation of intestinal stem cells.
885 *Journal of Clinical Investigation* **128**, 3806–3812 (2018).

886 53. Grivennikov, S. *et al.* IL-6 and Stat3 are required for survival of intestinal epithelial cells and
887 development of colitis-associated cancer. *Cancer Cell* **15**, 103–113 (2009).

888 54. Pickert, G. *et al.* STAT3 links IL-22 signaling in intestinal epithelial cells to mucosal wound
889 healing. *J Exp Med* **206**, 1465–1472 (2009).

890 55. Herrera, S. C. & Bach, E. A. JAK/STAT signaling in stem cells and regeneration: from
891 Drosophila to vertebrates. *Development* **146**, dev167643 (2019).

892 56. Biton, M. *et al.* T Helper Cell Cytokines Modulate Intestinal Stem Cell Renewal and
893 Differentiation. *Cell* **175**, 1307-1320.e22 (2018).

894 57. Van Unen, V. *et al.* Identification of a Disease-Associated Network of Intestinal Immune Cells
895 in Treatment-Naive Inflammatory Bowel Disease. *Front. Immunol.* **13**, 893803 (2022).

896 58. Oliver, A. J. *et al.* Single-cell integration reveals metaplasia in inflammatory gut diseases.
897 *Nature* **635**, 699–707 (2024).

898 59. Planell, N. *et al.* Transcriptional analysis of the intestinal mucosa of patients with ulcerative
899 colitis in remission reveals lasting epithelial cell alterations. *Gut* **62**, 967–976 (2013).

900 60. Friedrich, M. *et al.* IL-1-driven stromal-neutrophil interactions define a subset of patients with
901 inflammatory bowel disease that does not respond to therapies. *Nat Med* **27**, 1970–1981 (2021).

902 61. Li, J. *et al.* Identification and multimodal characterization of a specialized epithelial cell type
903 associated with Crohn's disease. *Nat Commun* **15**, 7204 (2024).

904 62. Arato, A., Savilahti, E. & Paszti, I. Crypt hyperplasia related to increased lymphocyte activation
905 in the rectal mucosa of children with ulcerative colitis. *Z Gastroenterol* **32**, 483–487 (1994).

906 63. Buczacki, S. J. A. *et al.* Intestinal label-retaining cells are secretory precursors expressing Lgr5.
907 *Nature* **495**, 65–69 (2013).

908 64. Nowell, C. S. *et al.* Chronic inflammation imposes aberrant cell fate in regenerating epithelia
909 through mechanotransduction. *Nat Cell Biol* **18**, 168–180 (2016).

910 65. Neurath, M. F., Pettersson, S., Meyer zum Büschenfelde, K. H. & Strober, W. Local
911 administration of antisense phosphorothioate oligonucleotides to the p65 subunit of NF-kappa B
912 abrogates established experimental colitis in mice. *Nat Med* **2**, 998–1004 (1996).

913 66. Rogler, G. *et al.* Nuclear factor kappaB is activated in macrophages and epithelial cells of
914 inflamed intestinal mucosa. *Gastroenterology* **115**, 357–369 (1998).

915 67. Schwitalla, S. *et al.* Intestinal Tumorigenesis Initiated by Dedifferentiation and Acquisition of
916 Stem-Cell-like Properties. *Cell* **152**, 25–38 (2013).

917 68. Myant, K. B. *et al.* ROS Production and NF-κB Activation Triggered by RAC1 Facilitate WNT-
918 Driven Intestinal Stem Cell Proliferation and Colorectal Cancer Initiation. *Cell Stem Cell* **12**, 761–773
919 (2013).

920 69. Jones, L. G. *et al.* NF-κB2 signalling in enteroids modulates enterocyte responses to secreted
921 factors from bone marrow-derived dendritic cells. *Cell Death Dis* **10**, 896 (2019).

70. Burkitt, M. D. *et al.* NF-κB1, NF-κB2 and c-Rel differentially regulate susceptibility to colitis-associated adenoma development in C57BL/6 mice. *J Pathol* **236**, 326–336 (2015).

71. Guo, Q. *et al.* NF-κB in biology and targeted therapy: new insights and translational implications. *Sig Transduct Target Ther* **9**, 53 (2024).

72. Yunshun Chen <Yuchen@Wehi. Edu.Au>, A. L. E. A. edgeR. Bioconductor https://doi.org/10.18129/B9.BIOC.EDGER (2017).

73. Gordon Smyth [Cre, A. limma. Bioconductor https://doi.org/10.18129/B9.BIOC.LIMMA (2017).

74. Hao, Y. *et al.* Dictionary learning for integrative, multimodal and scalable single-cell analysis. *Nat Biotechnol* **42**, 293–304 (2024).

75. Ordóñez-Morán, P., Dafflon, C., Imajo, M., Nishida, E. & Huelsken, J. HOXA5 Counteracts Stem Cell Traits by Inhibiting Wnt Signaling in Colorectal Cancer. *Cancer Cell* **28**, 815–829 (2015).

76. Hacker, D. L. & Ordóñez-Morán, P. Large-Scale Production of Recombinant Noggin and R-Spondin1 Proteins Required for the Maintenance of Stem Cells in Intestinal Organoid Cultures. *Methods Mol Biol* **2171**, 171–184 (2020).

77. Norkin, M., Ordóñez-Morán, P. & Huelsken, J. High-content, targeted RNA-seq screening in organoids for drug discovery in colorectal cancer. *Cell Rep* **35**, 109026 (2021).

78. Pleguezuelos-Manzano, C. *et al.* Establishment and Culture of Human Intestinal Organoids Derived from Adult Stem Cells. *Curr Protoc Immunol* **130**, e106 (2020).

Declarations

Ethics approval and consent to participate:

Human tissue samples were collected in accordance with the Declaration of Helsinki and with approval from the East Midlands - Leicester Central Research Ethics Committee under reference number [17/EM/0126, protocol 17015]. Written informed consent was obtained from all participants prior to sample collection. *Approval date: 02/07/2020*. Study title: Modelling Intestinal iNflammation and predIctinG response to therapies Using human enTeroids

All animal experiments were performed in accordance with institutional guidelines and approved by the Cantonal Veterinary Office Vaud, Switzerland under license number [VD1052/VD1053]. Approval date: 1/11/2015. Study title: Production and analysis of mouse models of cancer stem cells

Consent for publication: Not applicable

Clinical trial number: Not applicable.

954 **Availability of data and material**

955 The SPARC IBD data are available upon approved application to Crohn's & Colitis
956 Foundation IBD Plexus study (https://www.crohnscolitisfoundation.org/research/plexus).
957 PDOs bulk-RNAseq data and the code done for this manuscript is deposited in Github
958 Repository (https://github.com/brinda-bala/IBDstemcell.git).
959 The bulk RNA-seq data can be accessed here (GSE310845):
960 https://www.ncbi.nlm.nih.gov/geo/query/acc.cgi?acc=GSE310845

961 **Competing interests:**

962 C.P. is an AstraZeneca employee and AstraZeneca shareholder. P.O.M., G.M., and N.H.
963 receive research funding from AstraZeneca.

964 **Funding**

965 This work was supported by Medical Research Council (MRC) New Investigator Research
966 Award under grant number (MR/W01825X/1), Royal Society (RGS\R2\222116), CICRA
967 (RP/2020/2), GUTS UK (ECR2021_1), and the MRC Impact Accelerator Award
968 [MR/X502741/1].

969 **Authors' contributions**

970 P.O.M conceived, designed the study and wrote the manuscript with the help of B.B. P.O.M,
971 B.B., and S.P. analysed and interpret data. B.B. carried out the modelling work, model-data
972 comparison, RNAseq (single-cell and bulk) analyses, IBD Plexus analysis, experimental
973 approaches and produced the figures together with S.P. W.D performed sc-RNAseq analyses
974 by using Python. S.P performed mathematical tests, experimental approaches and
975 transcriptomic (RNAseq and microarrays) analyses. G.M. compiled and helped with patients'
976 stratification, samples and clinical input. P.O.M, B.B, S.P., L.G., W.D., L.G., N.H., J.H., C.P., and
977 G.M contributed to the discussions, interpretations and writing of the manuscript.

978 The authors declare that they have not use AI-generated work in this manuscript.

979 **Acknowledgements**

980 We would like to express our gratitude to the patients who generously participated in this study
981 and contributed their samples. We extend our sincere thanks to the nurses and clinical team
982 from Queen's Medical Centre (NIHR/NHS) Nottingham for their support and expertise in
983 sample collection. Their commitment and professionalism were invaluable in facilitating this
984 research. We would like to thank IBD Plexus team, US: the results published here are in part
985 based on data from the Study of a Prospective Adult Research Cohort with IBD (SPARC IBD)

986 **Materials & Correspondence**.

987 Correspondence and material requests should be addressed to P.O.M.

988

989 **Tables**

990 Table1-3.

991

992 **Figure legends**

993 **Figure 1. Epithelial cell heterogeneity profile varies with inflammation severity in IBD.**
994 (A) Bar plots showing the relative proportions of epithelial cell types stratified by endoscopic
995 inflammation scores in SPARC IBD-UC samples.
996 (B) Violin plots depicting significant differences in cell type proportions across macroscopic
997 appearance groups (normal, possible inflammation, inflammation).
998 (C) Violin plots of representative epithelial gene markers across the same macroscopic
999 groups.
1000 (D) Heatmap showing unsupervised clustering of epithelial marker genes based on
1001 macroscopic inflammation classification.
1002 (E) Heatmap (left) and spline curve (right) illustrating dynamic expression of epithelial

1003 markers over time in DSS-treated mice (GSE22307).

1004 (F) Violin plots of selected gene markers in the DSS-treated mouse model from the same

1005 dataset.

1006 (G) Dot plot of epithelial marker expression in single-cell RNA-seq data from DSS-treated

1007 mice (GSE264408), categorized by normal, acute, and chronic colitis.

1008 (H) Representative immunofluorescence images of mouse small intestine sections from

1009 control and DSS-treated animals stained for OLFM4 (red) and DAPI (blue). Yellow arrows

1010 indicate crypts. Images represent three independent biological replicates. Scale bar =

1011 100 μm.

1012

1013 **Figure 2. Characterization of epithelial cell alterations in IBD using a patient-derived**

1014 **organoid (PDO) model.**

1015 (A) Representative brightfield microscopy images of healthy (hPDOs) and IBD-derived PDOs

1016 (IBD-PDOs). Scale bar = 100 μm. Bulk RNA-seq analysis of hPDOs (n = 7, results of 2

1017 independent batches with early passage (n = 3, 3 independent wells) and late passage (n =

1018 4, 4 independent wells) and IBD-PDOs (n = 13, results of 3 independent donors, P89 (n = 4,

1019 4 independent wells), P90 (n = 3, 3 independent wells) and P99 (n = 6, results from 2

1020 independent batches with early passage (n = 3, 3 independent wells) and late passage (n =

1021 3, 3 independent wells).

1022 (B–C) Heatmaps showing expression of previously reported IBD-related markers (Dotti et al.

1023 2017) in hPDOs and IBD-PDOs: (b) downregulated and (c) upregulated genes.

1024 (D) Volcano plot of differentially expressed genes (DEGs) between hPDOs and IBD-PDOs

1025 (adjusted $p < 0.05$, $\log_2$ fold change > 5). Red dots represent significant DEGs; grey dots are

1026 non-significant. Total genes analysed: 26,771.

1027 (D) Heatmap of top DEGs distinguishing hPDOs from IBD-PDOs.

1028 (F) Bubble plot showing enriched pathways in IBD-PDOs vs hPDOs using Signaling Pathway

1029 Impact Analysis (SPIA).

1030 (G) Bar plot indicating estimated epithelial cell-type proportions in hPDOs and IBD-PDOs by

1031 computational deconvolution.

1032 (H) Bar plots showing mRNA expression levels of *LGR5*, *OLFM4*, and *CLU* in hPDOs (n = 4)

1033 and IBD-PDOs (n = 5). Results of 3 independent experiments.

1034 (I) Heatmap of selected epithelial gene markers in hPDOs and IBD-PDOs.

1035 (J) Brightfield images of hPDOs treated with IL-22 or vehicle control. Scale bar = 500 µm.

1036 Representative images from three independent biological replicates.

1037 (K) Bar graphs showing increased *OLFM4* and decreased *MUC2* mRNA expression in IL-22-

1038 treated hPDOs relative to control, as assessed by qPCR (n = 3) Results of 3 independent

1039 experiments.

1040

1041 **Figure 3. SC, TA and BEST4$^+$ epithelial subpopulations in healthy, non-inflamed, and**

1042 **inflamed UC tissue.**

1043 (A) UMAP embedding of epithelial cells from the reference dataset (Burclaff et al., 2022),

1044 annotated by cell type.

1045 (B) UMAP showing cell type predictions in the UC dataset (SCP259), highlighting SC/TA and

1046 BEST4$^+$ epithelial subpopulations.

1047 (C) Bar plot quantifying SC/TA and BEST4$^+$ cells across tissues with normal appearance,

1048 possible inflammation, and active inflammation.

1049 (D) UMAP displaying 19 transcriptionally distinct epithelial clusters (UC-C0 to UC-C18)

1050 identified in the UC dataset, indicating cellular heterogeneity within SC/TA and BEST4$^+$

1051 populations.

1052 (E–F) UMAPs annotated by (E) predicted cell type and (F) tissue health status.

1053 (G) Bar plot showing the distribution of UC clusters across epithelial cell types.

1054 (H) Bar plot showing the distribution of UC clusters by tissue health status.

1055 (I) Dot plot and (J) heatmap illustrating representative gene markers for biologically distinct
1056 epithelial clusters.
1057 (K) Feature plots showing expression of *PTTG1* and *UBE2C* in SC/TA and BEST4$^+$ cells
1058 within the UC dataset (SCP259), demonstrating transcriptional diversity across disease
1059 states.
1060 (L) Bar plot showing enriched pathways from Gene Ontology (GO-Biological Processes
1061 2023) for the top 50 genes in cluster UC-C1 (left), -C3 (middle) and –C12 (right).
1062

1063 **Figure 4. Immune-enriched gene clusters within SC, TA and BEST4$^+$ epithelial**
1064 **populations in inflamed UC.**
1065 (A) Bar plot showing enriched Hallmark gene sets from MSigDB for the top 50 genes in
1066 cluster UC-C18.
1067 (B) UMAP plots showing expression of selected UC-C18 marker genes (*ANXA1*, *REG4*,
1068 *TFF1*, *CD55*, *TIMP1*, and *PI3*) in SC/TA and BEST4$^+$ cells from the UC dataset (SCP259).
1069 (C) Dot plot showing expression of the selected UC-C18 markers across epithelial cells
1070 stratified by tissue source: healthy, non-inflamed UC, and inflamed UC (SCP259).
1071 (D) Dot plot showing expression of the same UC-C18 markers across SC, TA, and BEST4$^+$
1072 epithelial subtypes, stratified by tissue condition.
1073 (E) Heatmap showing average expression of UC-C18 marker genes across SPARC IBD-UC
1074 epithelial samples, stratified by macroscopic appearance (normal, possible inflammation, and
1075 inflammation).
1076 (F) Violin plots showing UC-C18 gene expression patterns in SPARC IBD-UC samples
1077 grouped by macroscopic appearance.
1078 (G) Spline curve showing average expression dynamics of UC-C18 marker genes in DSS-
1079 treated mouse colitis dataset (GSE22307).
1080 (H) Dot plot showing UC-C18 marker expression in SC, TA, and BEST4$^+$ populations from

1081 hPDOs treated with IL-22 or vehicle control (GSE189423).

1082 (I) Dot plot showing expression of UC-C18 markers stratified by LGR5 expression status in

1083 epithelial cells (GSE189423).

1084

1085 **Figure 5. A novel inflammation-linked gene signature associated with inflammation**

1086 **severity in IBD.**

1087 (A–C) Violin plots showing average expression of curated inflammatory genes (n = 476) in

1088 SPARC IBD-UC samples grouped by (A) disease activity, (B) macroscopic appearance, and

1089 (C) S100A9-based classification into normal (n = 747), possible inflammation (n = 141), and

1090 inflammation (n = 219) groups.

1091 (D) Representative confocal immunofluorescence images of S100A9 (red) and DAPI (blue)

1092 staining in inflamed and non-inflamed IBD tissues. Scale bar = 100 μm.

1093 (E) Venn diagram showing the intersection of significantly differentially expressed genes to

1094 define a 26-gene inflammation network in UC (26-GIN-UC).

1095 (F) Multidimensional scaling (MDS) plot showing sample distribution by gene expression

1096 profile across inflammation groups in the SPARC IBD-UC cohort.

1097 (G) Heatmap showing unsupervised clustering based on the 26-GIN-UC signature across the

1098 same cohort.

1099 (H) Significantly enriched pathways identified using Enrichr (MSigDB) from the 26-GIN-UC

1100 gene set.

1101 (I) Volcano plot showing differentially expressed proteins between inflamed and normal

1102 samples (red = significant proteins, adjusted $P < 0.05$; green = non-significant). Enriched

1103 upregulated (right) and downregulated (left) pathways are annotated from STRING analysis.

1104 (J–L) Heatmaps and spline curves showing dynamic expression of the 26-GIN-UC signature

1105 in DSS-treated mice from datasets: (J) GSE22307, (K) GSE214600, (L) GSE42768.

1106 P < 0.01 (**), P < 0.0001 (****).

1107

1108 **Figure 6. Adaptive epithelial responses in UC stratified by degree of inflammation.**

1109 (A) Spline curve showing the average expression of the 26-GIN-UC and UC-C18 gene

1110 signatures across increasing inflammation scores.

1111 (B–C) Box plots showing expression levels of (B) 26-GIN-UC and (C) UC-C18 gene

1112 signatures across low to high inflammation categories.

1113 (D) Spline curve (top) and box plot (bottom) of *S100A9* expression stratified by inflammation

1114 severity.

1115 (E–H) Spline curves (top) and box plots (bottom) showing gene expression across

1116 inflammation severity for (E) *LGR5*, (F) *OLFM4*, (G) *CLU*, and (H) *BEST4*.

1117 (I–L) Spline curves (top) and box plots (bottom) for epithelial differentiation and proliferation

1118 markers (I) *VIL1*, (J) *AVIL*, (K) *FABP1*, and (L) *PCNA* across inflammation categories.

1119

1120 **Figure 7. Integration of UC and CD sc-RNAseq data reveals distinct epithelial**

1121 **mechanisms of inflammation.**

1122 Differential gene expression and transcription factor pathway activation in DCS (A, B) and

1123 SCs (C, D) in Inflamed vs non-Inflamed groups.

1124 (E) Basic trajectory pseudotime analysis of the route from SCs to DCS. Taking the middle

1125 and late expressed genes in this trajectory (*KRT8*-early, *SCG5*-middle and *ANXA1*-late).

1126 (F) Bubble plot showing the expression of DCS trajectory related genes according to health

1127 status.

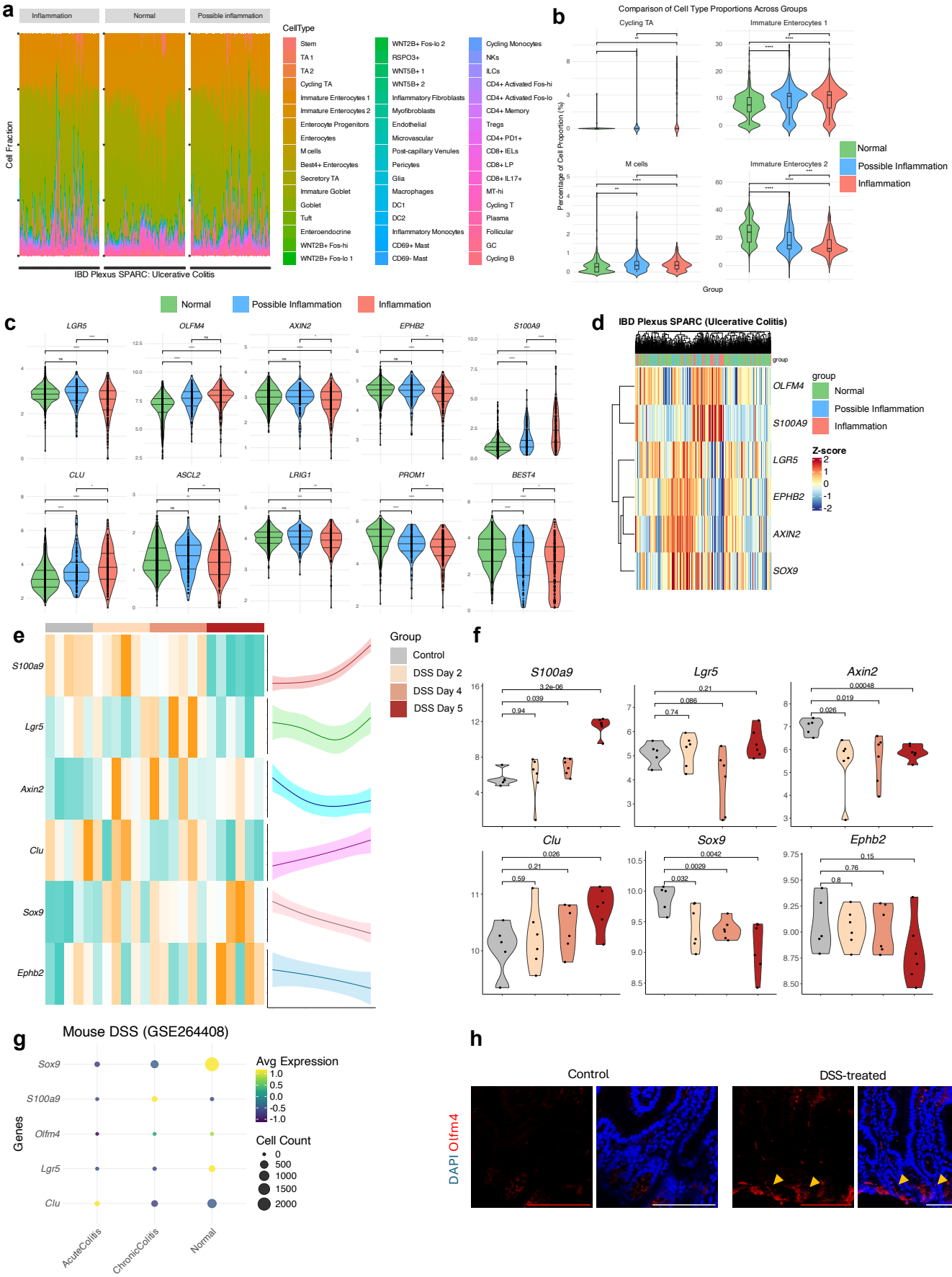
a
Inflammation
Normal
Possible inflammation
Cell Fraction
IBD Plexus SPARC: Ulcerative Colitis
CellType
Stem
TA 1
TA 2
Cycling TA
Immature Enterocytes 1
Immature Enterocytes 2
Enterocyte Progenitors
Enterocytes
M cells
Best4+ Enterocytes
Secretory TA
Immature Goblet
Goblet
Tuft
Enteroendocrine
WNT2B+ Fos-hi
WNT2B+ Fos-lo 1
WNT2B+ Fos-lo 2
RSPO3+
WNT5B+ 1
WNT5B+ 2
Inflammatory Fibroblasts
Myofibroblasts
Endothelial
Microvascular
Post-capillary Venules
Pericytes
Glia
Macrophages
DC1
DC2
Inflammatory Monocytes
CD69+ Mast
CD69- Mast
Cycling Monocytes
NKs
ILCs
CD4+ Activated Fos-hi
CD4+ Activated Fos-lo
CD4+ Memory
Tregs
CD4+ PD1+
CD8+ IELs
CD8+ LP
CD8+ IL17+
MT-hi
Cycling T
Plasma
Follicular
GC
Cycling B
b
Comparison of Cell Type Proportions Across Groups
Cycling TA
Immature Enterocytes 1
M cells
Immature Enterocytes 2
Percentage of Cell Proportion (%)
Group
Normal
Possible Inflammation
Inflammation
c
Normal
Possible Inflammation
Inflammation
LGR5
OLFM4
AXIN2
EPHB2
S100A9
CLU
ASCL2
LRIG1
PROM1
BEST4
d
IBD Plexus SPARC (Ulcerative Colitis)
group
OLFM4
S100A9
LGR5
EPHB2
AXIN2
SOX9
group
Normal
Possible Inflammation
Inflammation
Z-score
2
1
0
-1
-2
e
S100a9
Lgr5
Axin2
Clu
Sox9
Ephb2
Group
Control
DSS Day 2
DSS Day 4
DSS Day 5
f
S100a9
Lgr5
Axin2
Clu
Sox9
Ephb2
g
Mouse DSS (GSE264408)
Genes
Sox9
S100a9
Olfm4
Lgr5
Clu
AcuteColitis
ChronicColitis
Normal
Avg Expression
1.0
0.5
0.0
-0.5
-1.0
Cell Count
0
500
1000
1500
2000
h
Control
DSS-treated
DAPI Olfm4

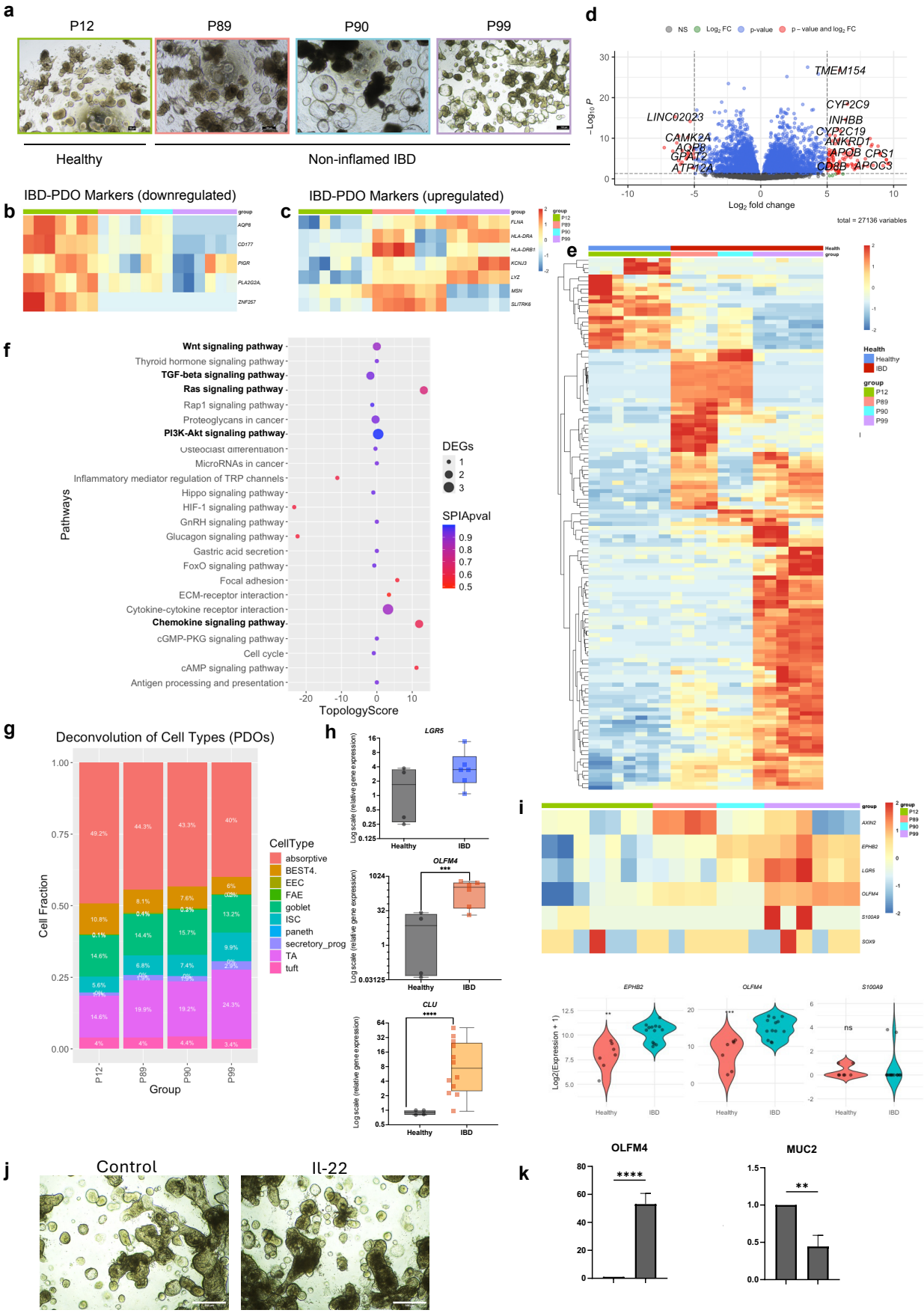
a
P12
P89
P90
P99
Healthy
Non-inflamed IBD
b
IBD-PDO Markers (downregulated)
c
IBD-PDO Markers (upregulated)
d
NS
Log2 FC
p-value
p – value and log2 FC
TMEM154
CYP2C9
INHBB
CYP2C19
ANKRD1
APOB
CPS1
APOC3
LINC02023
CAMK2A
AQP8
GPAT2
ATP12A
Log2 fold change
total = 27136 variables
e
Health
Healthy
IBD
group
P12
P89
P90
P99
f
Wnt signaling pathway
Thyroid hormone signaling pathway
TGF-beta signaling pathway
Ras signaling pathway
Rap1 signaling pathway
Proteoglycans in cancer
PI3K-Akt signaling pathway
Osteoclast differentiation
MicroRNAs in cancer
Inflammatory mediator regulation of TRP channels
Hippo signaling pathway
HIF-1 signaling pathway
GnRH signaling pathway
Glucagon signaling pathway
Gastric acid secretion
FoxO signaling pathway
Focal adhesion
ECM-receptor interaction
Cytokine-cytokine receptor interaction
Chemokine signaling pathway
cGMP-PKG signaling pathway
Cell cycle
cAMP signaling pathway
Antigen processing and presentation
Pathways
TopologyScore
DEGs
SPIApval
g
Deconvolution of Cell Types (PDOs)
Cell Fraction
Group
CellType
absorptive
BEST4.
EEC
FAE
goblet
ISC
paneth
secretory_prog
TA
tuft
h
LGR5
OLFM4
CLU
Log scale (relative gene expression)
Healthy
IBD
i
AXIN2
EPHB2
LGR5
OLFM4
S100A9
SOX9
Log2(Expression + 1)
ns
j
Control
Il-22
k
OLFM4
MUC2

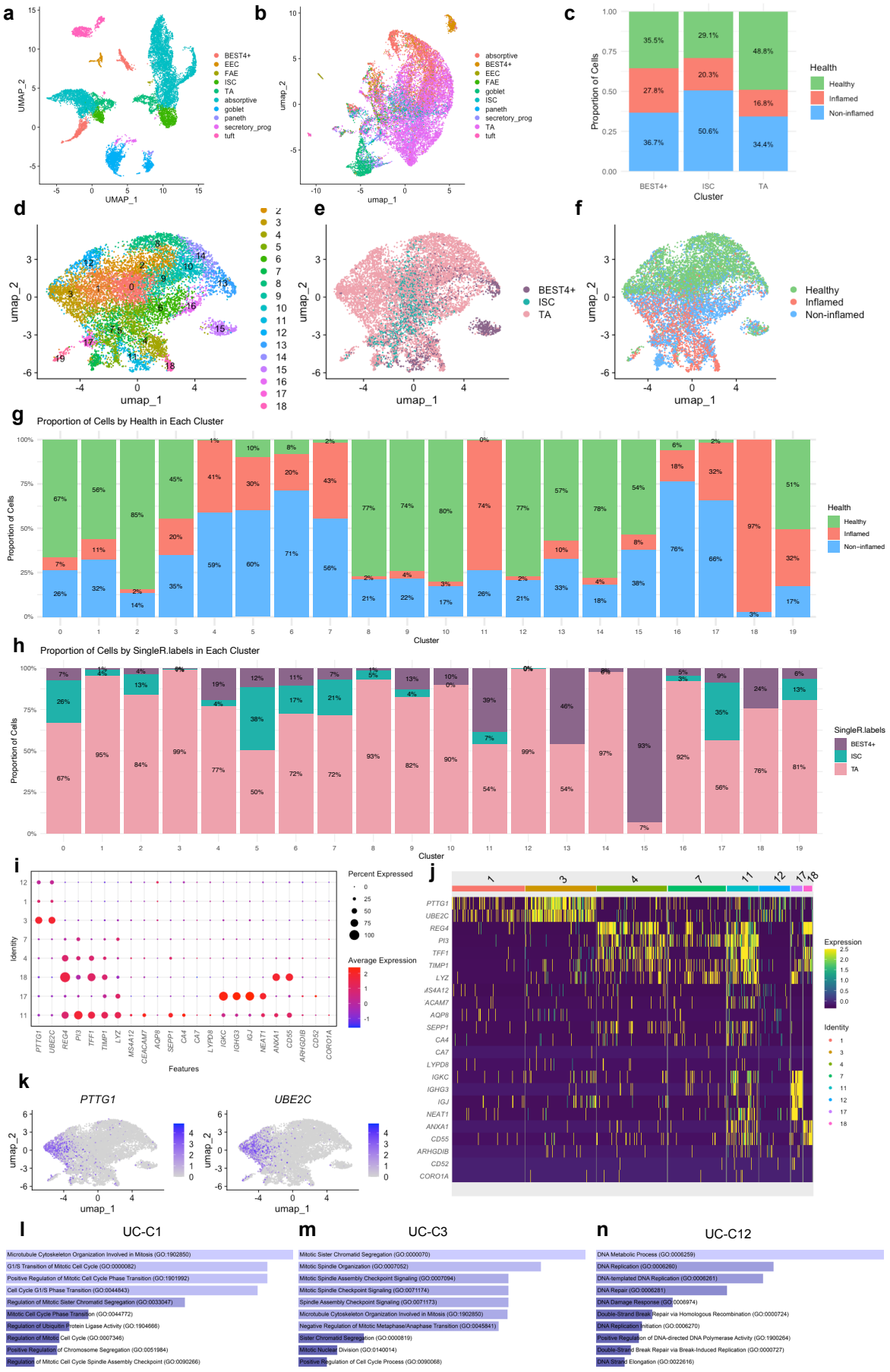
a
UMAP_2
UMAP_1
BEST4+
EEC
FAE
ISC
TA
absorptive
goblet
paneth
secretory_prog
tuft
b
umap_2
umap_1
absorptive
BEST4+
EEC
FAE
goblet
ISC
paneth
secretory_prog
TA
tuft
c
Proportion of Cells
Cluster
BEST4+
ISC
TA
35.5%
27.8%
36.7%
29.1%
20.3%
50.6%
48.8%
16.8%
34.4%
Health
Healthy
Inflamed
Non-inflamed
d
umap_2
umap_1
e
BEST4+
ISC
TA
f
Healthy
Inflamed
Non-inflamed
g
Proportion of Cells by Health in Each Cluster
Proportion of Cells
Cluster
Health
Healthy
Inflamed
Non-inflamed
h
Proportion of Cells by SingleR.labels in Each Cluster
Proportion of Cells
Cluster
SingleR.labels
BEST4+
ISC
TA
i
Identity
Features
PTTG1
UBE2C
REG4
PI3
TFF1
TIMP1
LYZ
MS4A12
CEACAM7
AQP8
SEPP1
CA4
CA7
LYPD8
IGKC
IGHG3
IGJ
NEAT1
ANXA1
CD55
ARHGDIB
CD52
CORO1A
Percent Expressed
Average Expression
j
Expression
Identity
k
PTTG1
UBE2C
umap_2
umap_1
l
UC-C1
Microtubule Cytoskeleton Organization Involved in Mitosis (GO:1902850)
G1/S Transition of Mitotic Cell Cycle (GO:0000082)
Positive Regulation of Mitotic Cell Cycle Phase Transition (GO:1901992)
Cell Cycle G1/S Phase Transition (GO:0044843)
Regulation of Mitotic Sister Chromatid Segregation (GO:0033047)
Mitotic Cell Cycle Phase Transition (GO:0044772)
Regulation of Ubiquitin Protein Ligase Activity (GO:1904666)
Regulation of Mitotic Cell Cycle (GO:0007346)
Positive Regulation of Chromosome Segregation (GO:0051984)
Regulation of Mitotic Cell Cycle Spindle Assembly Checkpoint (GO:0090266)
m
UC-C3
Mitotic Sister Chromatid Segregation (GO:0000070)
Mitotic Spindle Organization (GO:0007052)
Mitotic Spindle Assembly Checkpoint Signaling (GO:0007094)
Mitotic Spindle Checkpoint Signaling (GO:0071174)
Spindle Assembly Checkpoint Signaling (GO:0071173)
Microtubule Cytoskeleton Organization Involved in Mitosis (GO:1902850)
Negative Regulation of Mitotic Metaphase/Anaphase Transition (GO:0045841)
Sister Chromatid Segregation (GO:0000819)
Mitotic Nuclear Division (GO:0140014)
Positive Regulation of Cell Cycle Process (GO:0090068)
n
UC-C12
DNA Metabolic Process (GO:0006259)
DNA Replication (GO:0006260)
DNA-templated DNA Replication (GO:0006261)
DNA Repair (GO:0006281)
DNA Damage Response (GO:0006974)
Double-Strand Break Repair via Homologous Recombination (GO:0000724)
DNA Replication Initiation (GO:0006270)
Positive Regulation of DNA-directed DNA Polymerase Activity (GO:1900264)
Double-Strand Break Repair via Break-Induced Replication (GO:0000727)
DNA Strand Elongation (GO:0022616)

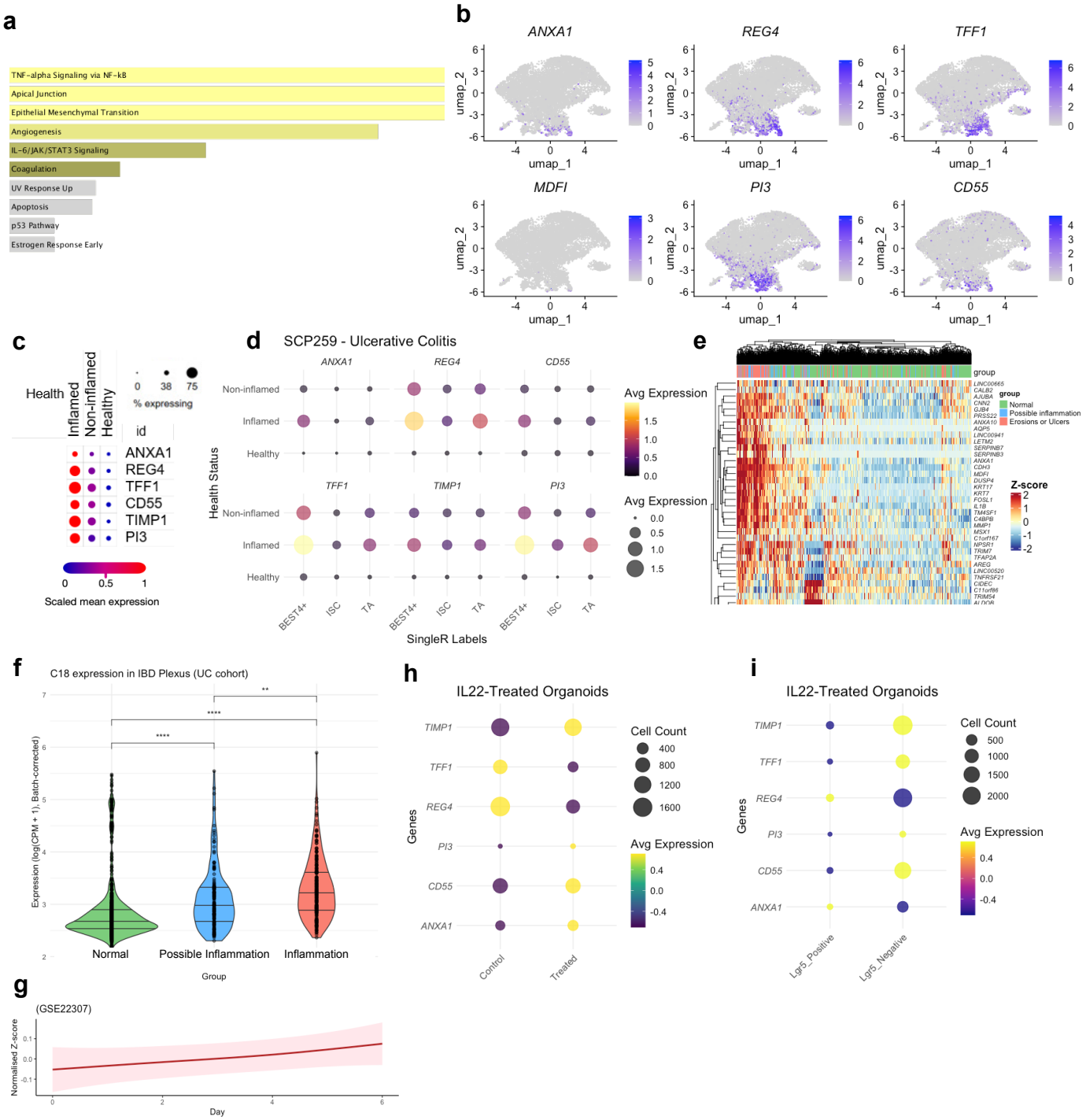
a
TNF-alpha Signaling via NF-kB
Apical Junction
Epithelial Mesenchymal Transition
Angiogenesis
IL-6/JAK/STAT3 Signaling
Coagulation
UV Response Up
Apoptosis
p53 Pathway
Estrogen Response Early
b
ANXA1
REG4
TFF1
MDFI
PI3
CD55
umap_1
umap_2
c
Health
Inflamed
Non-inflamed
Healthy
% expressing
id
ANXA1
REG4
TFF1
CD55
TIMP1
PI3
Scaled mean expression
d
SCP259 - Ulcerative Colitis
Health Status
Non-inflamed
Inflamed
Healthy
Avg Expression
BEST4+
ISC
TA
SingleR Labels
e
group
Normal
Possible inflammation
Erosions or Ulcers
Z-score
f
C18 expression in IBD Plexus (UC cohort)
Expression (log(CPM + 1), Batch-corrected)
Normal
Possible Inflammation
Inflammation
Group
g
(GSE22307)
Normalised Z-score
Day
h
IL22-Treated Organoids
Genes
Cell Count
Avg Expression
Control
Treated
i
IL22-Treated Organoids
Lgr5_Positive
Lgr5_Negative

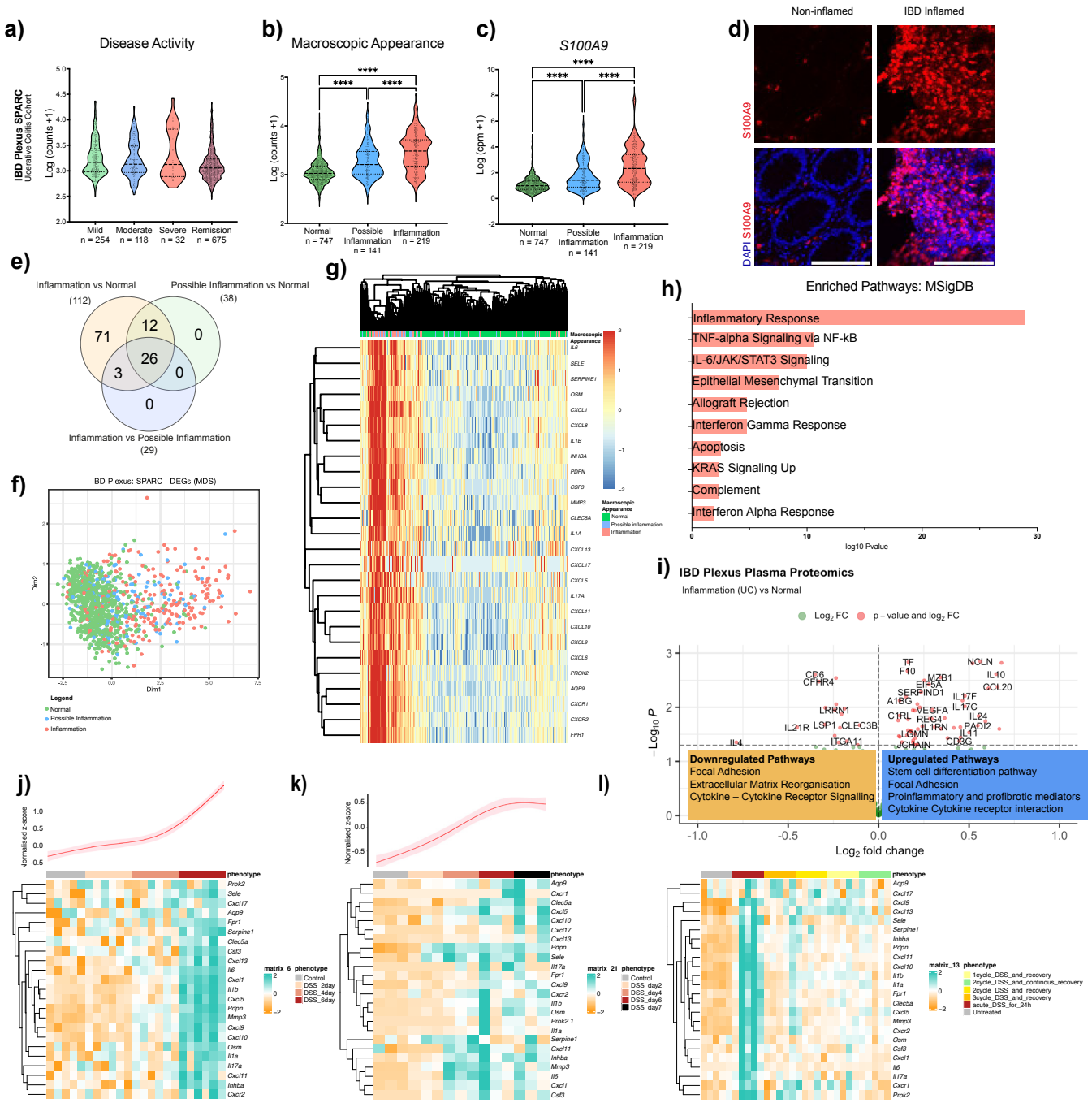
a)
Disease Activity
IBD Plexus SPARC
Ulcerative Colitis Cohort
Log (counts +1)
Mild n = 254
Moderate n = 118
Severe n = 32
Remission n = 675
b)
Macroscopic Appearance
Log (counts +1)
Normal n = 747
Possible Inflammation n = 141
Inflammation n = 219
c)
S100A9
Log (cpm +1)
Normal n = 747
Possible Inflammation n = 141
Inflammation n = 219
d)
Non-inflamed
IBD Inflamed
S100A9
DAPI S100A9
e)
Inflammation vs Normal (112)
Possible Inflammation vs Normal (38)
Inflammation vs Possible Inflammation (29)
71
12
0
26
3
0
0
f)
IBD Plexus: SPARC - DEGs (MDS)
Dim1
Dim2
Legend
Normal
Possible Inflammation
Inflammation
g)
Macroscopic Appearance
Normal
Possible Inflammation
Inflammation
h)
Enriched Pathways: MSigDB
Inflammatory Response
TNF-alpha Signaling via NF-kB
IL-6/JAK/STAT3 Signaling
Epithelial Mesenchymal Transition
Allograft Rejection
Interferon Gamma Response
Apoptosis
KRAS Signaling Up
Complement
Interferon Alpha Response
- log10 Pvalue
i)
IBD Plexus Plasma Proteomics
Inflammation (UC) vs Normal
Log2 FC
p – value and log2 FC
Downregulated Pathways
Focal Adhesion
Extracellular Matrix Reorganisation
Cytokine – Cytokine Receptor Signalling
Upregulated Pathways
Stem cell differentiation pathway
Focal Adhesion
Proinflammatory and profibrotic mediators
Cytokine Cytokine receptor interaction
Log2 fold change
j)
k)
l)
phenotype
Control
DSS_2day
DSS_4day
DSS_6day
DSS_day2
DSS_day4
DSS_day6
DSS_day7
1cycle_DSS_and_recovery
2cycle_DSS_and_continous_recovery
2cycle_DSS_and_recovery
3cycle_DSS_and_recovery
acute_DSS_for_24h
Untreated

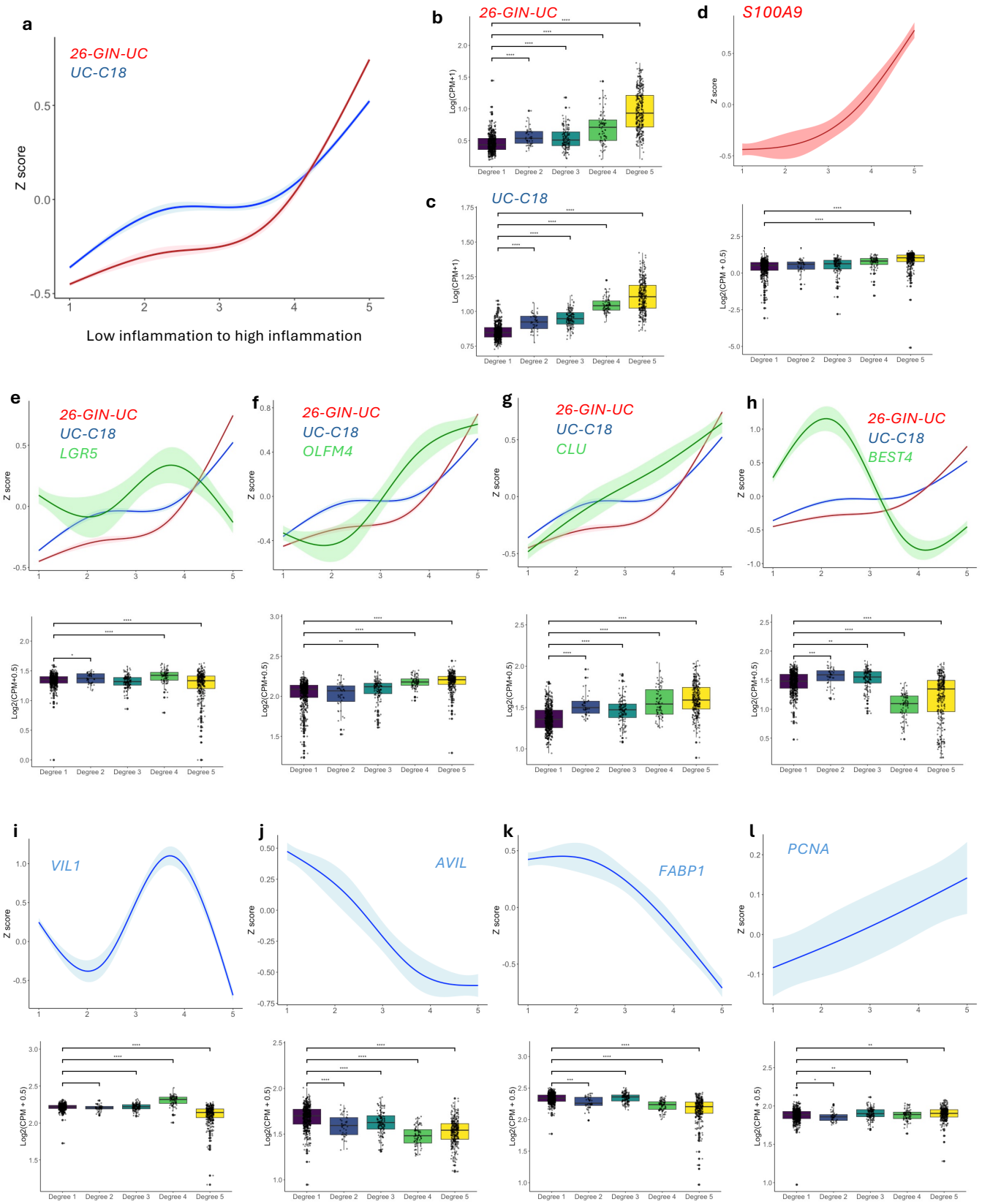
a
26-GIN-UC
UC-C18
Z score
Low inflammation to high inflammation
b
26-GIN-UC
Log(CPM+1)
Degree 1
Degree 2
Degree 3
Degree 4
Degree 5
c
UC-C18
Log(CPM+1)
d
S100A9
Z score
Log2(CPM + 0.5)
e
26-GIN-UC
UC-C18
LGR5
f
26-GIN-UC
UC-C18
OLFM4
g
26-GIN-UC
UC-C18
CLU
h
26-GIN-UC
UC-C18
BEST4
Log2(CPM+0.5)
i
VIL1
j
AVIL
k
FABP1
l
PCNA

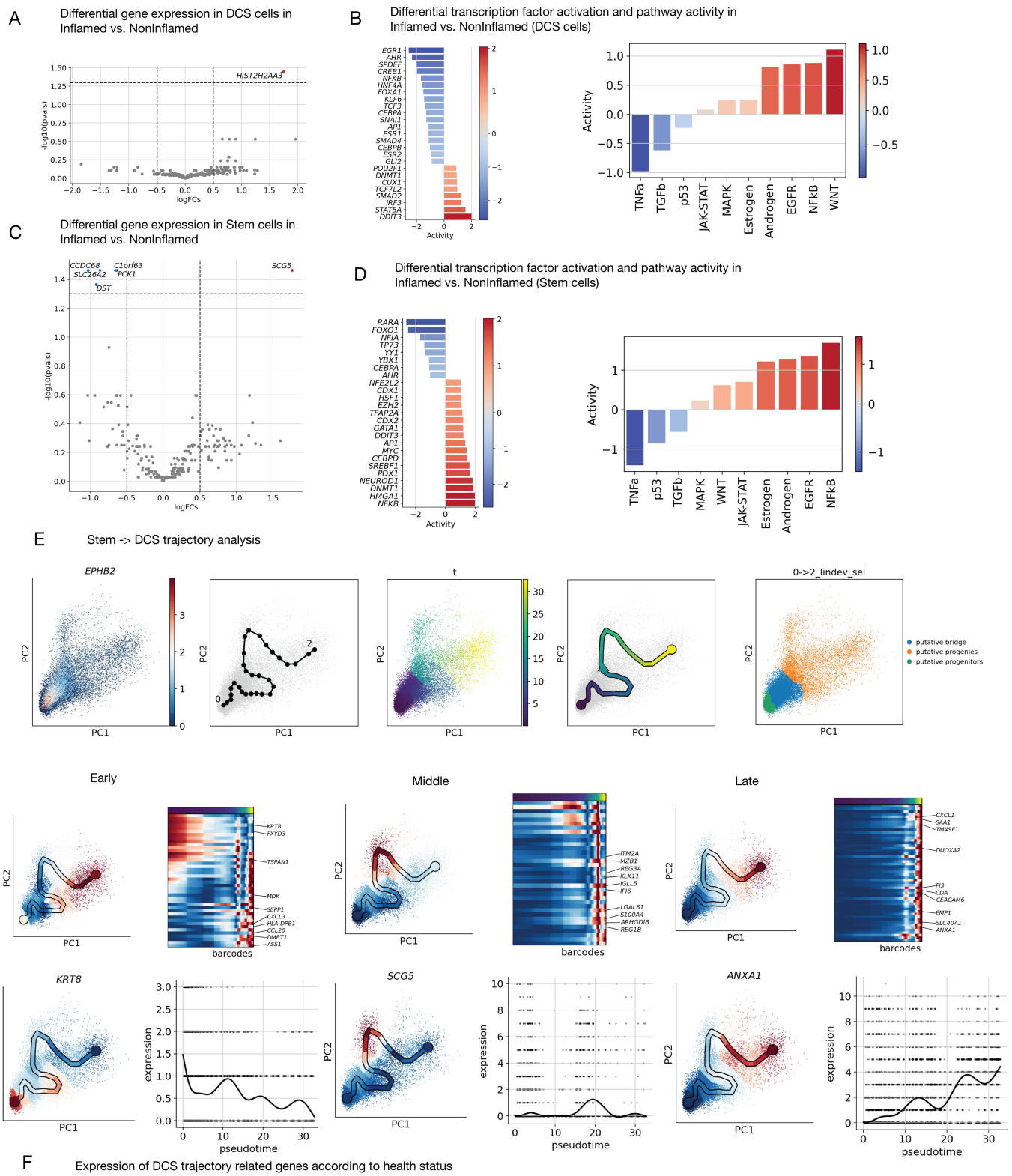
A
Differential gene expression in DCS cells in Inflamed vs. NonInflamed
HIST2H2AA3
-log10(pvals)
logFCs
B
Differential transcription factor activation and pathway activity in Inflamed vs. NonInflamed (DCS cells)
EGR1
AHR
SPDEF
CREB1
NFKB
HNF4A
FOXA1
KLF6
TCF3
CEBPA
SNAI1
AP1
ESR1
SMAD4
CEBPB
ESR2
GLI2
POU2F1
DNMT1
CUX1
TCF7L2
SMAD2
IRF3
STAT5A
DDIT3
Activity
TNFa
TGFb
p53
JAK-STAT
MAPK
Estrogen
Androgen
EGFR
NFkB
WNT
C
Differential gene expression in Stem cells in Inflamed vs. NonInflamed
CCDC68
C1orf63
SLC26A2
PCK1
DST
SCG5
-log10(pvals)
logFCs
D
Differential transcription factor activation and pathway activity in Inflamed vs. NonInflamed (Stem cells)
RARA
FOXO1
NFIA
TP73
YY1
YBX1
CEBPA
AHR
NFE2L2
CDX1
HSF1
EZH2
TFAP2A
CDX2
GATA1
DDIT3
AP1
MYC
CEBPD
SREBF1
PDX1
NEUROD1
DNMT1
HMGA1
NFKB
Activity
TNFa
p53
TGFb
MAPK
WNT
JAK-STAT
Estrogen
Androgen
EGFR
NFkB
E
Stem -> DCS trajectory analysis
EPHB2
t
0->2_lindev_sel
PC1
PC2
putative bridge
putative progenies
putative progenitors
Early
Middle
Late
KRT8
FXYD3
TSPAN1
MDK
SEPP1
CXCL3
HLA-DPB1
CCL20
DMBT1
ASS1
barcodes
ITM2A
MZB1
REG3A
KLK11
IGLL5
IFI6
LGALS1
S100A4
ARHGDIB
REG1B
CXCL1
SAA1
TM4SF1
DUOXA2
P3
CDA
CEACAM6
EMP1
SLC40A1
ANXA1
expression
pseudotime
SCG5
ANXA1
F
Expression of DCS trajectory related genes according to health status
Healthy
Inflamed_CD
Inflamed_UC
NoninflamedUC
NoninflamedCD
Fraction of cells in group (%)
Mean expression in group